Interfacial Layers of Small Molecule Organic Solar Cells

Sure Nagendra Babu

(EE15MTECH11013)

A Dissertation Submitted to

Indian Institute of Technology Hyderabad

In Partial Fulfillment of the Requirements for

The Degree of Master of Technology

भारतीय प्रौद्योगिकी संस्थान हैदराबाद

Indian Institute of Technology Hyderabad

Department of Electrical Engineering

December, 2017

Declaration

I declare that this written submission represents my ideas in my own words, and where others' ideas or words have been included, I have adequately cited and referenced the original sources. I also declare that I have adhered to all principles of academic honesty and integrity and have not misrepresented or fabricated or falsified any idea/data/fact/source in my submission. I understand that any violation of the above will be a cause for disciplinary action by the Institute and can also evoke penal action from the sources that have thus not been properly cited, or from whom proper permission has not been taken when needed.

Nagendra

(Signature)

Sure Nagendra Babu

(– Student Name –)

EE15MTECH11013

(Roll No)

Approval Sheet

This thesis entitled "Interfacial Layers of Small Molecule Organic Solar Cells" by Sure Nagendra Babu is approved for the degree of Master of Technology from IIT Hyderabad.

18/12/17

Dr. Sai Santosh Kumar Raavi

-Name and affiliation- Dept. Physics

Examiner

18/12/2017.

-Name and affiliation- Dr. Kamlesh Nayak

Examiner

Swati 18/12/2017

-Name and affiliation- Dr. Swati Gupta

Adviser Assistant Prof.

18/12/17.

-Name and affiliation-

DR. AMIT ACHARYYA
ASSOCIATE PROFESSOR.

Chairman

Acknowledgements

Firstly, I want to sincerely acknowledge my supervisor, Dr. Swati Gupta, Assistant professor in IIT Hyderabad for her continuous support, guidance and encouragement during the entire thesis work. She has involved me in different areas of development of organic solar cells such as modeling, fabrication and characterization. This enhanced my scope of understanding about research and development. She encouraged me to attend talks and events during my thesis. M.Suresh who was a PhD student in our research group has helped me by providing masks for fabrication.

Furthermore, I want to acknowledge Centre for Nano Science and Engineering (CeNSE), Indian Institute of Science (IISc), Bengaluru for providing fabrication and characterization facilities under Indian Nanoelectronics Users Program (INUP). S.Sabiha, who was process integrator for me in CeNSE arranged facilities whenever requested. Members of photovoltaics lab, R.Dwarakanathan, T.Veeramani and Reshma have operated the equipments during fabrication of organic solar cells.

Abstract

The influence of interfacial layers, introduced between electrodes and active layer, on organic solar cells was understood. Anode interfacial layer was made of vanadium oxide (V_2O_5) or 4,4′,4″-Tris[phenyl(m-tolyl)amino]triphenylamine (m-MTDATA). V_2O_5 is an inorganic material and m-MTDATA is an organic material. Tris(8-hydroxyquinolinato)aluminium (Alq_3) was chosen as cathode interfacial layer. Two thicknesses of 5 nm and 10 nm were considered for each of V_2O_5, m-MTDATA and Alq_3. Modeling and simulation of devices was done using transfer matrix methodology for the measurement of optical electric field, device reflectance, power dissipation, absorptance and power re-distribution. Optical and electrical characterization of fabricated devices was done for the measurement of current density-voltage characteristics, device reflectance, thickness, refractive index and extinction coefficient. It was observed that device with m-MTDATA of 5 nm as anode interfacial layer and Alq_3 of 5 nm as cathode interfacial layer resulted in better performance.

.

Contents

Chapter 1

Introduction

In this chapter, section 1.1 describes the importance of sources of renewable energy. Section 1.2 explains about the motivation for this thesis. Section 1.3 discusses about the solar cells and their classification into three generations. Section 1.4 mentions the thesis objective. Section 1.5 gives the thesis outline and section 1.6 presents the thesis contribution.

1.1 Renewable energy

The energy sources that can be replenished and will never run out are known as renewable energy sources. Some examples of renewable energy sources are: solar, wind, bio-power, tidal, geo-thermal and small hydro power. Solar energy is one of the most potential renewable energy sources owing to its free and abundant nature of availability.

As per International Energy Outlook (2016), world energy consumption projected to be expanded by 48 per cent from 2012 to 2040 [1]. In order to meet this energy demands in a sustainable and environment-friendly way, harnessing solar energy is an urgent requirement at large scale.

Solar energy is a potential alternative to fossil fuels such as coal, petroleum and natural gas. The issues such as non-renewability and green house gas emissions from the fossil fuel sources can be overcome using solar energy.

Solar energy can be converted into electrical energy by solar panels. This electrical energy can be utilized in operating solar water pumps (agriculture), solar panels

(residential and industrial usage), solar-powered vehicles (transport) and solar panels for satellites and spacecrafts (space). Other modes of energy include petrol, diesel, natural gas and coal based thermal energy. These modes of energy are non-renewable in nature and not environment-friendly since they are fossil fuels.

This thesis focuses on development of efficient organic solar cell to convert solar energy into electrical energy.

1.2 Motivation

Based on Figure 1.1, it is evident that percentage of renewable energy sources to India's energy sector is only 17 per cent and that of fossil fuel energy sources is 67 per cent. Also, there is mismatch between demand and supply of energy in India [2]. From Figure 1.2, it can be observed that solar energy contribution to India's energy sector is less than 10 per cent.

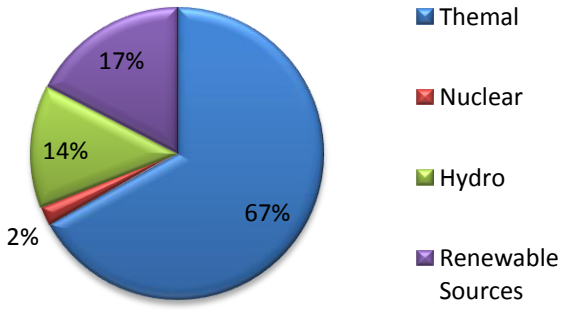

Figure 1.1: Installed capacity of energy sources in India (as of April 2017) [3]

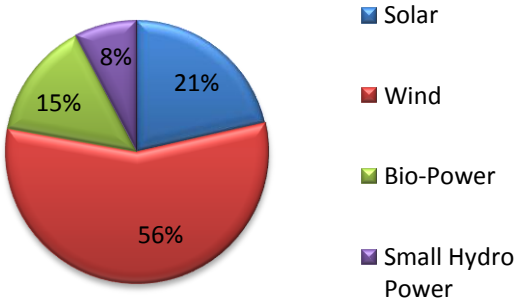

Figure 1.2: Installed capacity of renewable energy sources in India (as of March 2017) [3]

Low contribution of solar energy to India's energy sector and high dependence on fossil fuel energy sources motivated me to pursue research in the field of solar energy. The percentage of solar energy can be increased by developing low-cost technology based on organic semiconductors which will be explained in the next section.

1.3 Solar cells

Solar cells convert solar energy into electrical energy which can be used in various sectors such as agricultural, industrial, residential and transportation. Solar cells work on the principle of photovoltaic effect which was firstly observed by Edmond Becquerel, a French scientist in 1839 [4]. In 1883, first solar cell was fabricated by using silicon material. The commercial production of silicon based solar cells started from 1950s. Later, research focused on non-silicon based materials such as Cadmium Telluride (CdTe) and Copper Indium Gallium diSelenide (CIGS) for lowering cost of production of solar cells. These different solar cell technologies can be classified into three generations.

First generation solar cells are based mono-crystalline silicon and poly-crystalline silicon. Second generation solar cells are based on thin-film technologies such as cadmium telluride (CdTe), copper indium gallium diselenide (CIGS) and amorphous silicon. Third generation solar cells are emerging ones and they include organic solar cells, dye-sensitized solar cells and perovskite solar cells.

1.4 Thesis objective

Organic solar cell (OSC) consists of active layer (donor and acceptor) sandwiched between cathode and anode along with anode and cathode interfacial layers as shown in Figure 1.3. The donor and acceptor are organic semiconducting materials which are responsible for conversion of solar energy into electrical energy. In order to improve charge collection at electrodes, anode and cathode interfacial layer is introduced between anode/donor and cathode/acceptor, respectively.

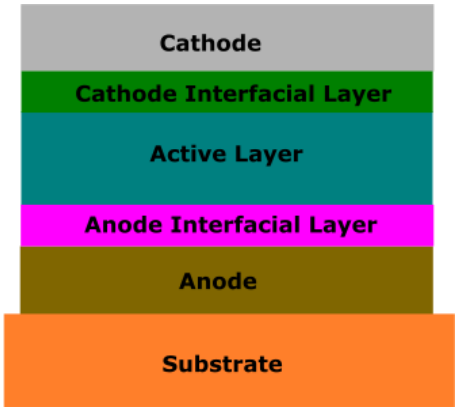

Figure 1.3: Schematic of an organic solar cell

In this thesis work, research is focused on anode and cathode interfacial layer. The objective is to understand the influence of thickness of interfacial layer on performance of small molecule organic solar cell (SMOSC). Further, the comparison of inorganic and organic anode interface layer is studied.

1.5 Thesis outline

The thesis consists of experimental and modeling aspects of development of robust interfacial layer at anode and cathode. Chapter 2 explains of charge transport properties of organic semiconductors, history and configurations of organic solar cells, working principle and role of various layers in organic solar cells. Chapter 3 describes methodologies related to modeling, fabrication, and characterization. Chapter 4 presents the influence of anode interfacial layer on performance of SMOSC. Similarly, chapter 5 presents the effects of thickness of cathode interfacial layer on the performance of SMOSC. The conclusions and future scope of thesis is explained in the following chapter.

1.6 Thesis contribution

This thesis contributed in developing efficient and stable organic solar cells by selecting appropriate materials of optimum thickness for various layers. The active layer thickness is optimized by considering the maximum light absorption within the active layer. The charge collection was improved by introducing interfacial layers.

References

[1] U.S. Energy Information Administration, *International Energy Outlook 2016*, 0484(2016).

[2] "Power Sector at a Glance ALL INDIA | Government of India | Ministry of Power." [Online]. Available: http://powermin.nic.in/en/content/power-sector-glance-all-india. [Accessed: 08-Nov-2017].

[3] Central Electricity Authority, "All India Installed Capacity of Power Stations," *Ministry of Power, Government of India*, 2017. [Online]. Available: http://www.cea.nic.in/reports/monthly/installedcapacity/2016/installed_capacity-06.pdf.

[4] Alyssa Baker, "History of Solar Cells: How Technology Has Evolved | Solar Power Authority," 2016. [Online]. Available: https://www.solarpowerauthority.com/a-history-of-solar-cells/. [Accessed: 10-Jun-2017].

Chapter 2

Organic Solar Cells

In this chapter, section 2.1 describes types, deposition methods, and optical and electronic properties of organic semiconductors. Section 2.2 explains organic electronic devices such as organic thin film transistors, organic solar cells, organic photodetectors and organic light emitting diodes. The working principle and the history of organic solar cells are presented in section 2.3 and 2.4, respectively. Section 2.5 discusses configurations of organic solar cells. The role of active layer, electrodes and interfacial layers in organic solar cells are explained in section 2.6. The figures of merit for performance and the literature review are included in section 2.7 and 2.8, respectively.

2.1 Organic semiconductors

Organic semiconductors are π-conjugated molecules which contain alternating single and double bonds. They mainly consists of carbon and hydrogen atoms. In some materials sulfur, oxygen, and nitrogen are also introduced. For example, copper phthalocyanine (CuPc) has nitrogen atoms as shown in Figure 2.1 (a). Organic molecules are covalently coupled and held together by Van-der-Waals interactions.

Organic semiconductor materials are broadly classified into two groups, polymers and small molecules. Copper phthalocyanine (CuPc) and poly(3-hexylthiophene-2,5-diyl) (P3HT) are one of the examples of small molecules and polymer as shown in Figure 2.1 (a) and (b), respectively.

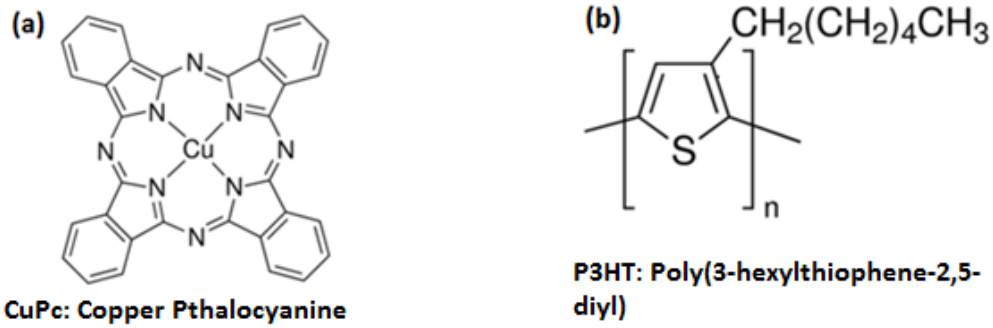

Figure 2.1: Example of (a) small molecule and (b) polymer organic semiconductor

2.1.1 Deposition of organic materials

The depositions techniques can be broadly classified into dry techniques and wet techniques. Dry techniques are vacuum thermal evaporation and vapor phase deposition. While wet techniques are spin coating, ink-jet printing, spray-coating, stamping and screen-printing. In wet techniques, solute is dissolved in solvent. To have good uniformity of films, solute must be highly dissolved in solvents. On the other hand, dry techniques are solvent-free processing which also provides better thickness control and faster processing. Usually small molecules are deposited by dry techniques and polymers by solution-processing. Organic materials are deposited using vacuum thermal evaporation technique in our all experiments.

2.1.2 Optical and electronic properties of organic semiconductors

The electronic configuration of carbon atom is $1s^2$ $2s^2$ $2p^2$. In the ground state as depicted in Figure 2.2 (a), one 2s orbital is completely filled and two of three 2p orbital are partially filled. In the excited state as shown in Figure 2.2 (b), one electron of 2s orbital excites to remaining 2p orbital. In organic semiconducting materials, carbon is in sp^2 hybridization due to mixing of 2s orbital and two 2p orbital in the excited state presented in Figure 2.2 (c). Three sp^2 hybrid orbitals form a triangle within a plane and remaining unhybridized p orbital (p_z) is in perpendicular to this plane. The side and top views of sp^2 hybridized carbon atoms are shown in Figure 2.2 (d) and (e) respectively. This p_z orbital forms π-bond with p_z orbital of another carbon atom as depicted in Figure 2.3. π-bond gives rise to new energy levels known as, highest occupied molecular orbital (HOMO) and lowest

unoccupied molecular orbital (LUMO). The moderate energy gap organic materials can be used as semiconducting layer in the device. It leads to various applications as explained in next section.

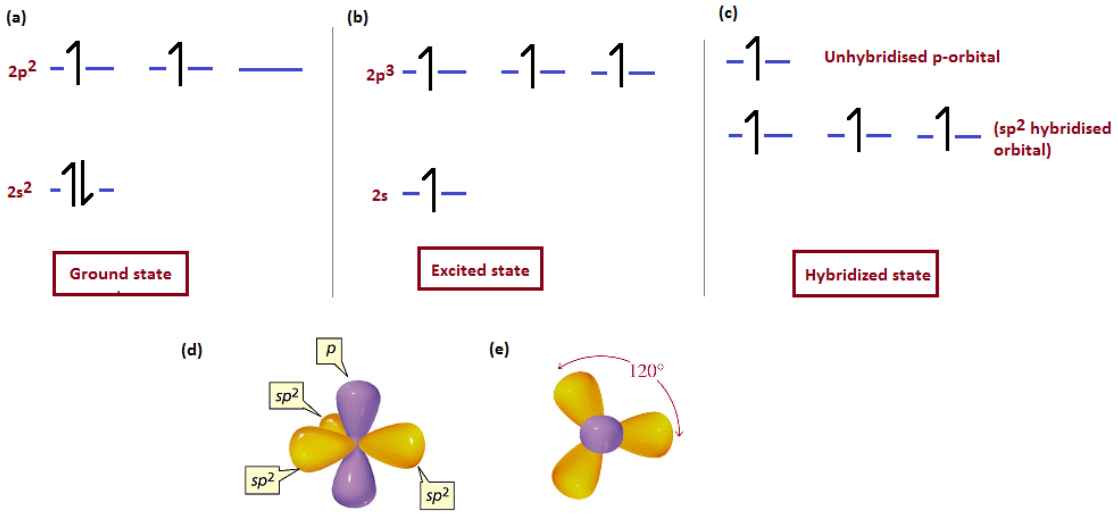

Figure 2.2: (a) ground state; (b) excited state; (c) hybridized sp^2 carbon atom; (d) side view and (e) top view of hybridized carbon atom

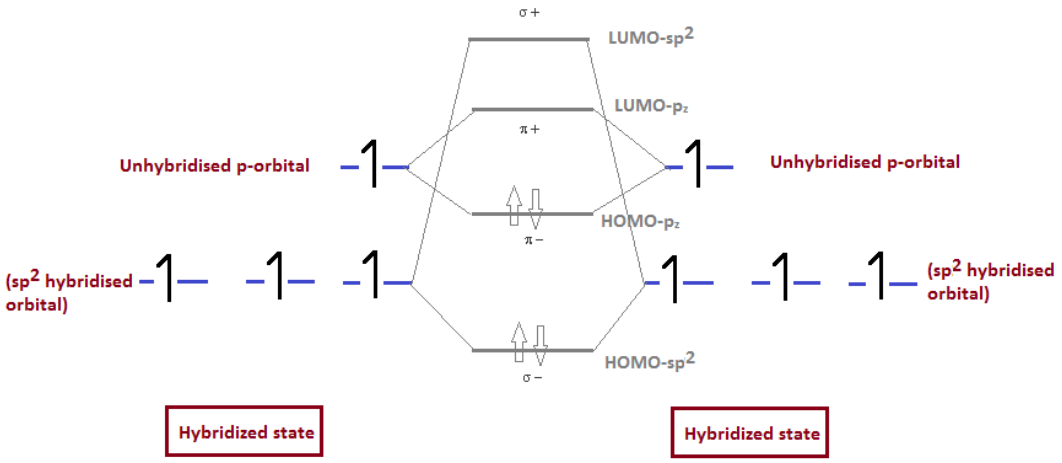

Figure 2.3: HOMO and LUMO formation due to bonding of two sp^2 hybridized atoms

2.2 Organic electronic devices

The low-cost fabrication methods, good charge transport and optical properties opened the possibilities to use them in most of the electronic devices. Some of the devices are described below:

Organic thin film transistors (OTFTs): The advantage of low processing temperature and low cost fabrication on various substrates such as glass and plastic

makes OTFTs attractive candidates over conventional silicon based transistors. But because of their low-field mobility, OTFTs have limited applications in smart cards, sensor, radio frequency identification tags (RFID), e-paper, and flat panel displays [5], [6].

Organic solar cells (OSCs): In order to meet rising energy demands using renewable sources of energy such as organic solar cells are potential candidates [7]. Currently, silicon based solar cells are dominantly used and their efficiencies is around 25.3 percent [8]. But still research in organic solar cells is emerging because of low temperature processing, fabrication on flexible and plastic substrates, availability of transparent devices and less material consumption. All these advantages of organic solar cells drive towards low-cost solar cells. But two main challenges in the development or commercialization of organic solar cells are low efficiency and less stability.

The energy band gap of an organic semiconductor is typically between 1 and 3 eV [9]. Therefore they can absorb light of 300-700 nm wavelengths which lead to their applications in solar cells and LEDs. For example, copper phthalocyanine (CuPc) is an organic semiconducting material with energy band gap of 1.7 eV. The energies range in visible spectrum is 1.8 eV to 3.1 eV. Therefore, CuPc absorbs most of the visible spectrum wavelengths and it is used light absorbing layer in organic solar cells.

Organic light emitting diodes (OLEDs): Light emitting diodes emit light in response to an electric current. OLEDs provides advantages over liquid crystal display (LCDs) and conventional LEDs, due to their self-emitting property, brightness, speed, wide viewing angle, low power consumption, and contrast [10].

Organic photo detectors (OPDs): Large area detectors are possible using printed electronic techniques such as roll-to-roll processing, inkjet printing and spray-coating. By fabricating OPDs on plastic, paper or glass can be transformed into intelligent surfaces [11].

In this thesis work, organic solar cells were developed on glass substrates by using thermal evaporation.

2.3 Working principle of organic solar cells

Conversion of solar energy into electrical energy includes of exciton generation, exciton dissociation, and charge collection at the electrodes. The overall efficiency is the product of absorption efficiency (η_A), dissociation efficiency (η_D), and charge collection efficiency (η_{cc}). Absorption of incident light in the active layer results in generation of bounded electron-hole pair (exciton) as illustrated in step 1 of Figure 2.4. In organic molecules, frenkel excitons with strong columbic force due to low relative permittivity are present. While because of high dielectric constant of silicon, wannier-mott excitons are present.

Excitons diffuse within the material and they can either dissociate into electrons and holes at the interface or recombine before reaching the interface. Excitons diffusion and dissociation are shown as step 2 and step 3, respectively in Figure 2.4. In heterojuction organic solar cells, the difference in LUMO energy levels of donor and acceptor acts as driving force for exciton dissociation. The separated electrons and holes are transported as illustrated in the step 4. As shown in step 5, electrons and holes are collected by cathode and anode, respectively. If the exciton diffusion length is small, then the probability of recombination is higher than dissociation.

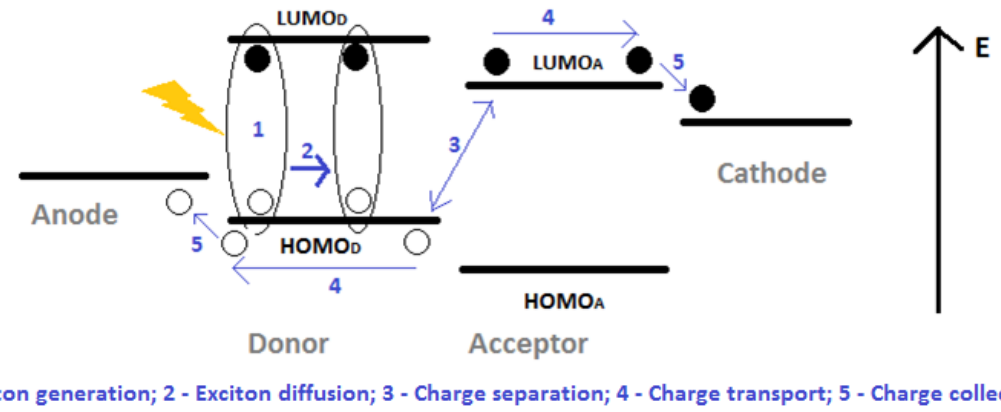

Figure 2.4: Schematic of working of a heterojunction organic solar cell. Open circles represents holes; filled circles represents electrons; ellipse represents bounded hole-electron pair (exciton); yellow symbol represents incidence of light and E represents the energy scale.

2.4 History of organic solar cells

In 1959, Kallaman and Pope [12] reported photovoltaic effect using a single crystal of anthracene which was sandwiched between two similar electrodes consisting of NaCl solution and silver electrodes. The single layer device (as shown in Figure 2.5(a)) requires less material but it leads to very low efficiencies, because of poor exciton dissociation [13]. In 1986, Tang et. al. [14] demonstrated the first single heterojunction organic solar cell, in which active layer consists of two materials named as donor and acceptor as shown in Figure 2.5 (b). The interface between acceptor and donor enhanced exciton dissociation efficiency. In 1991, Hiramoto [15] proposed the first bulk heterojunction photovoltaic device by co-sublimation. This bulk heterojunction device schematic represented in Figure 2.6 resulted in increased interfacial areas as compared to planar heterojunction devices. In this device structure, the overall efficiency is function of morphology of bulk heterojunction layer. In order to have broader absorption, first multi-junction solar cell structure was demostrated by Bedair et al. [16], [17]. The active layer materials have complementary absorption spectrum to absorb photons of broader wavelengths. Recently, ternary organic solar cells are gaining research attention owing to broadened absorption range of organic solar cells as an alternative to tandem cell structures [18]. This structure includes three materials of different band gaps in a single active layer.

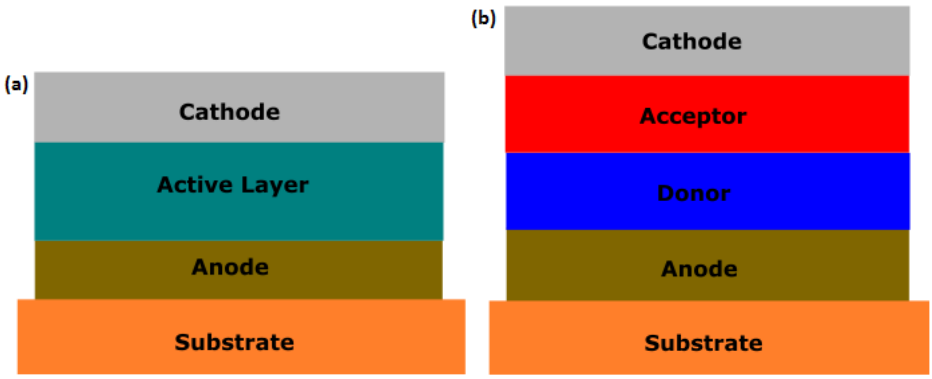

Figure 2.5: (a) Single material based organic solar cell and (b) Single heterojunction organic solar cell

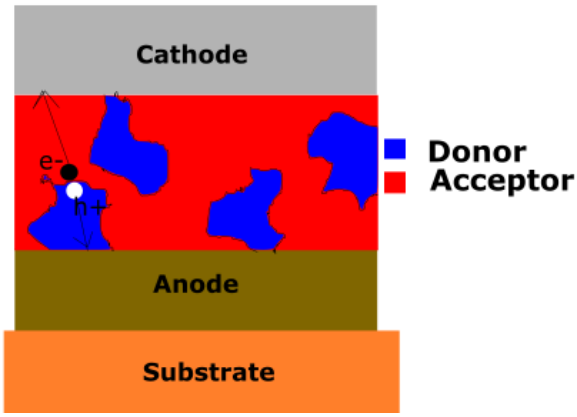

Figure 2.6: Bulk heterojunction organic solar cell proposed by Hiramoto [15]

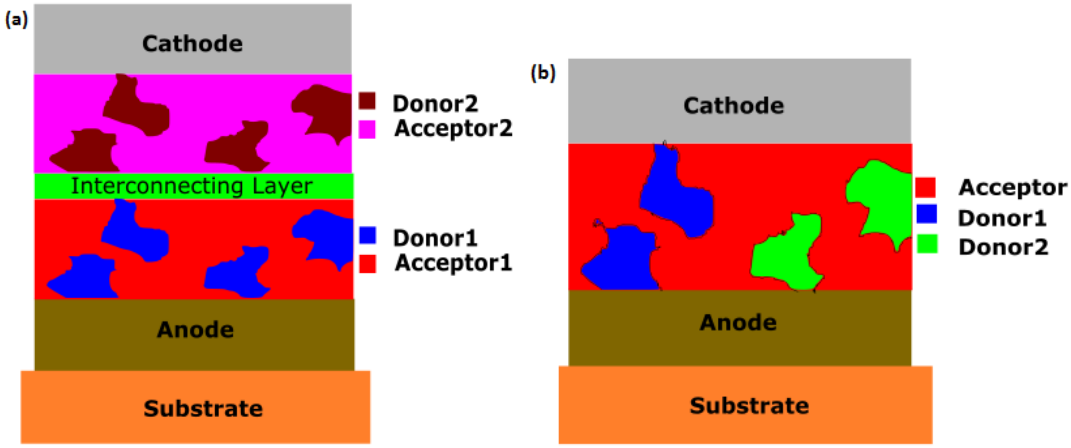

Figure 2.7: Schematic of (a) tandem organic solar cell and (b) ternary organic solar cell

2.5 Configurations of organic solar cells

Two configurations of organic solar cells: conventional and inverted are demonstrated in Figure 2.8 (a) and (b), respectively. A basic structure of organic solar cell consists of anode, active layer and cathode. In conventional devices, holes are collected on substrate side whereas in inverted devices, electrons are collected at the substrate side. Conventional solar cells provide better efficiency than inverted configuration based devices but relatively less stability. The top layer of inverted device is made of high work-function material which provides more air stability.

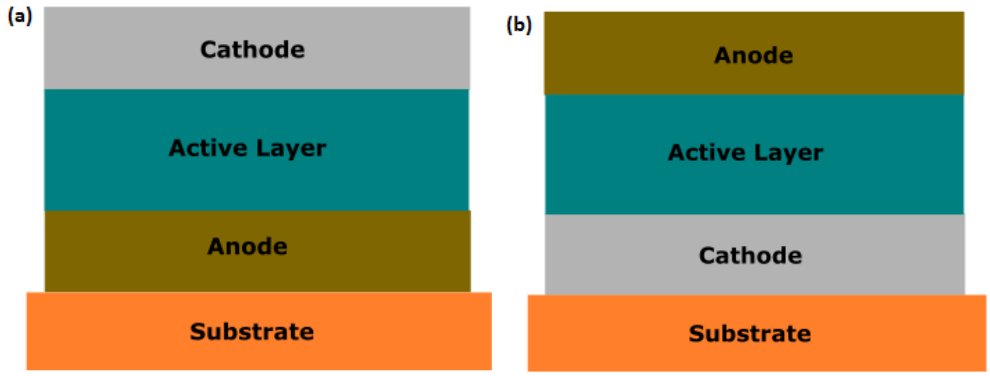

Figure 2.8: Schematic of (a) conventional organic solar cell and (b) inverted organic solar cells

2.6 Role of different layers

A schematic of an organic solar cell including cathode, anode, anode interfacial layer, cathode interfacial layer and active layer is shown in Figure 2.9. Each layer of organic solar cell has specific role in the device operation as explained below.

2.6.1 Active layer

The active layer is composed of organic semiconductor materials. Photons are absorbed by the active layer materials and therefore low bandgap materials are preferred. Depending on relative HOMO and LUMO levels, they are named as donor and acceptor materials. Donor provides electrons and acceptor accepts electrons. In early devices, active layer was made of one semiconducting material while in later devices, it consists of minimum of two organic materials. In heterojunction solar cell, generated excitions are dissociated at donor/acceptor interface.

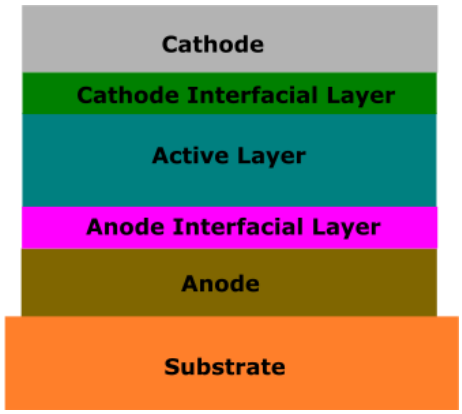

Figure 2.9: Schematic of an organic solar cell with interfacial layers

2.6.2 Electrodes

The separated charge carriers from the active layer are collected by electrodes. Anode and cathode collect holes and electrons, respectively.

2.6.3 Interfacial layers

Interfacial layers are present between electrodes and active layer. The interfacial layer at anode side is termed as anode interfacial layer (AIL) while at cathode side as cathode interfacial layer (CIL). Anode interfacial layer improves holes collection at anode by blocking exciton and electron transport to anode.

2.7 Figures of merit

The current-voltage characteristics of a typical solar cell in dark and light conditions are presented in Figure 2.10. The performances of different solar cells are compared by their values of power conversion efficiency, short-circuit current density, open-circuit voltage and fill factor

(a) Open-circuit voltage (V_{OC}): It is the maximum voltage available from a solar cell and it is measured under open circuit condition.

(b) Short-circuit current (I_{SC}): It is the maximum current in the device and it is measured under short circuit condition.

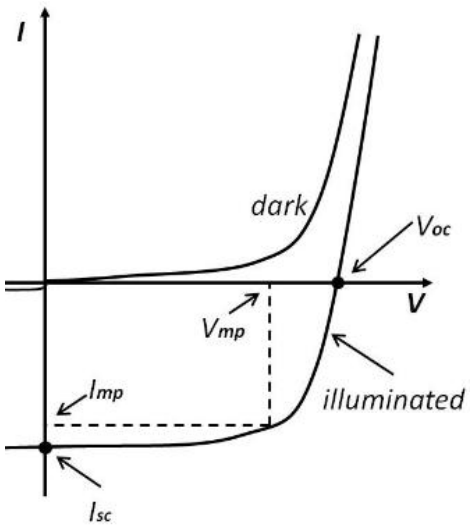

Figure 2.10: Current-voltage characteristics of a solar cell under dark and illumination conditions [19]

(c) Fill factor (FF): It is defined as the ratio of the maximum power from the solar cell to the product of V_{OC} and I_{SC}. It also tells about the extent of squareness of the I-V curve of the device. The maximum fill factor is one when the I-V curve is a rectangle.

$$FF = \frac{V_{mp}\, I_{mp}}{V_{OC}\, I_{SC}}$$

V_{mp} and I_{mp} are the voltage and current corresponding to the maximum power point of solar cell. Series resistance (R_s) and shunt resistance (R_{sh}) affects the fill factor. Ideally series resistance should be zero and shunt resistance should be infinite.

(d) Efficiency: It is the ratio of maximum output power to the input power.

$$\eta = \frac{V_{OC} I_{SC} FF}{P_{in}}$$

(e) Stability or lifetime: It is a measure of change in of electrical characteristics (I-V, efficiency) of the device with time. In organic solar cells degradation can be due to factors such as exposure to ambient oxygen and water vapor and long-term light exposure [20].

2.8 Literature review

Organic solar cells can be fabricated using low-cost processing techniques. Organic materials offer high absorption efficiencies, flexibility, and transparency. These advantages of organic solar cells make them more attractive for research. But their commercialization is limited because of low power conversion efficiency and poor long-term reliability. Introducing interfacial layer or buffer layer between anode and donor/acceptor layer contributes to enhancement of efficiency and stability in organic solar cells.

For example, L.Cattin et al. reported surface passivation of the anode and improvement in efficiency using ultra thin molybdenum oxide (MoO_3) as anode interfacial layer (AIL) [21]. Pao-Hsun Huang et al. used double anode buffer layers (MoO_3 and pentacene) in CuPc:C60 based active layer configuration in order to

improve reliability and efficiency [22]. Similarly, A. R. Yu et al. reported improvement in efficiency by depressing the dissociation of excitons introduction of double AIL [23]. Yongbiao Zhao et al. reported efficient and stable hole injection by MoO_3 and PEDOT:PSS as AIL [24]. Quinn Burlingame et al. used TPBi:C70 materials between cathode and active layer as cathode interfacial layer [25].

Interfacial layers are not limited to only organic solar cells. For example, in organic thin film transistors (OTFTs), vanadium oxide (V_2O_5) [5] and 4,4',4''- Tris[(3-methylphenyl) -phenylamino]triphenylamine (m-MTDATA) [6] were used as interfacial layers in order to decrease contact resistance and improve hole mobility. These same materials were used as interfacial layers in organic light emitting diodes (OLEDs) [26], [27] also in order to improve hole injection from electrodes to active layer.

We implemented m-MTDATA or V_2O_5 as anode interfacial layer materials in organic solar cell based on small molecules: copper phthalocyanine (CuPc) and buckminster fullerene (C_{60}). The effect of anode interfacial layer on the performance of organic solar cells was investigated. The optimum thickness of m-MTDATA and V_2O_5 were determined from the modeling and experiments. The influence of cathode interfacial layer (Alq3) on the performance of CuPc:C60 organic solar cell was also briefly understood by varying thickness.

References

[1] C. W. Chu, S. H. Li, C. W. Chen, V. Shrotriya, and Y. Yang, "High-performance organic thin-film transistors with metal oxide/metal bilayer electrode," *Appl. Phys. Lett.*, 87(2005), pp. 1-3.

[2] S.-H. Su, C.-M. Wu, S.-Y. Kung, and M. Yokoyama, "Enhancing the performance of organic thin-film transistors using an organic-doped inorganic buffer layer," *Thin Solid Films*, 536(2013), pp. 229–234.

[3] Z. Yin, J. Wei, and Q. Zheng, "Interfacial Materials for Organic Solar Cells:

Recent Advances and Perspectives," *Adv. Sci.*, 3(2016), pp. 1–37.

[4] NREL, "Best Research-Cell Efficiencies," 2017. [Online]. Available: https://www.nrel.gov/pv/assets/images/efficiency-chart.png. [Accessed: 10-Jun-2017].

[5] W. Brütting, "Organic Semiconductors," *Semiconductors*, 6(2005), pp. 1–11.

[6] A. Islam, M. Rabbani, M. H. Bappy, M. A. R. Miah, and N. Sakib, "A review on fabrication process of organic light emitting diodes," *2013 Int. Conf. Informatics, Electron. Vis.*, 2013.

[7] M. Kielar, O. Dhez, G. Pecastaings, A. Curutchet, and L. Hirsch, "Long-Term Stable Organic Photodetectors with Ultra Low Dark Currents for High Detectivity Applications," *Sci. Rep.*, 6(2016), p. 39201.

[8] H. Kallmann and M. Pope, "Photovoltaic Effect in Organic Crystals," *J. Chem. Phys.*, 30,(1959), pp. 585–586.

[9] V. W. W. Yam, *WOLEDs and organic photovoltaics : recent advances and applications*. Springer, 2010.

[10] C. W. Tang, "Two-layer organic photovoltaic cell," *Appl. Phys. Lett.*, 48(1986), pp. 183–185.

[11] M. Hiramoto, H. Fujiwara, M. Yokoyama, M. Hiramoto, H. Fujiwara, and M. Yokoyama, "Threelayered organic solar cell with a photoactive interlayer of codeposited pigments Three-layered organic solar cell with a photoactive of codeposited pigments," 1062(1991).

[12] C. C. Chen *et al.*, "An efficient triple-junction polymer solar cell having a power conversion efficiency exceeding 11%," *Adv. Mater.*, 26(2014), pp. 5670–5677.

[13] R. K. Jones, J. H. Ermer, C. M. Fetzer, and R. R. King, "Evolution of multijunction solar cell technology for concentrating photovoltaics," *Jpn. J.*

Appl. Phys., 51(2012).

[14] G. Zhang *et al.*, "High-Performance Ternary Organic Solar Cell Enabled by a Thick Active Layer Containing a Liquid Crystalline Small Molecule Donor," *J. Am. Chem. Soc.*, 139(2017) pp. 2387–2395.

[15] P. Sidi, D. Sukoco, W. Purnomo, H. Sudibyo, and D. Hartanto, "Electric Energy Management and Engineering in Solar Cell System," in *Solar Cells - Research and Application Perspectives*, InTech, 2013.

[16] V. L. Dalal, R. Mayer, J. Bhattacharya, and M. Samiee, "Stability of organic solar cells," *2012 IEEE Int. Reliab. Phys. Symp.*, 2012.

[17] L. Cattin *et al.*, "MoO3 surface passivation of the transparent anode in organic solar cells using ultrathin films," *J. Appl. Phys.*, 105(2009).

[18] P. Huang, C. Huang, K. Chen, J. Ke, Y. Wang, and C. Kang, "Improved Reliability of Small Molecule Organic Solar Cells by Double Anode Buffer Layers," 2014.

[19] A. R. Yu *et al.*, "Experimental evidence of harmful exciton dissociation at MoO_3 /CuPc interface in OPV," *J. Appl. Phys.*, 120(2016) p. 145501.

[20] Y. Zhao, J. Chen, W. Chen, and D. Ma, "Poly(3,4-ethylenedioxythiophene):Poly(styrenesulfonate)/MoO 3 composite layer for efficient and stable hole injection in organic semiconductors," *J. Appl. Phys.*, 111(2012), pp. 1–6.

[21] Q. Burlingame *et al.*, "Reliability of Small Molecule Organic Photovoltaics with Electron-Filtering Compound Buffer Layers," *Adv. Energy Mater.*, 6(2016), pp. 1–11.

[22] A. Kuruvila *et al.*, "Organic light emitting diodes with environmentally and thermally stable doped graphene electrodes," *J. Mater. Chem. C*, 2(2014) p. 6940.

[23] G. T. L, D. X. L, W. F. M, J. W, W. J. Y, and L. Z. Q, "Optical and Electrical Properties of OLED with the Structure of ITO/ m-MTDATA/Meo-TPD/Alq $_3$ /LiF/Al," *J. Phys. Conf. Ser.*, 276(2011), p. 12076.

Chapter 3

Methodology

Section 3.1 describes transfer matrix approach, a method of optical modeling which is used to determine optical electric field distribution and reflectance within various layers of optical devices. Section 3.2 explains fabrication methods. The involved characterization methods are included in section 3.3.

3.1 Optical modeling

A solar cell converts solar energy to electrical energy. In order to achieve higher efficiency, the optical electric field and power dissipation must be maximized within the active layer among various layers of a solar cell. The distribution of these parameters depends on thickness, refractive index, and extinction coefficient of each layer. In this thesis, optical modeling was performed to determine the optimum thickness of various layers by using transfer matrix approach. Reflectance, power dissipation, absorptance and power redistribution were obtained from modeling.

3.1.1 Transfer matrix method

It was first demonstrated for optical modeling of organic solar cell by Pettersson et al [1]. Each material is considered as one layer and a device can have finite number of n layers as show in Figure 3.1. The interaction of light at the interface is governed by snell's law as given in equation 3.1.

$$\boldsymbol{n_1} * \sin \theta_i = \boldsymbol{n_2} * \sin \theta_t \tag{3.1}$$

n_1 and n_2 is refractive index of medium 1 and medium 2. θ_i and θ_t are incident and transmit angles, respectively. These parameters are illustrated in Figure 3.2.

When light is incident on the interface of two different media, some part of incident light is reflected back into the same medium and other part is refracted in another medium.

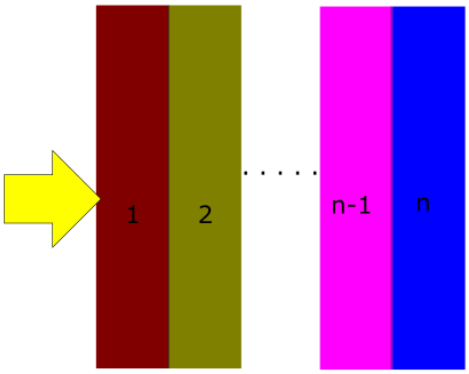

Figure 3.1: A multi-layer device with layers indexed as 1,2...n and arrow showing direction of incident light

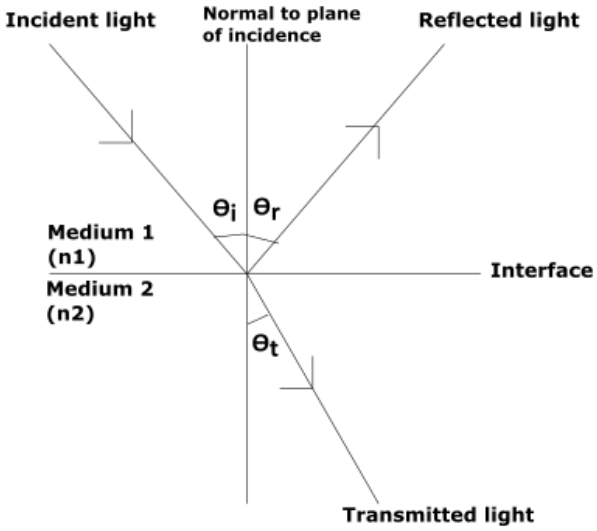

Figure 3.2: Illustration of light incidence on interface of two medium 1 and medium 2 where n_1 and n_2 are refractive indices of respective medium; θ_i, θ_r and θ_t are angle of incidence, reflectance and transmittance respectively

The percentage of reflection or transmission is determined by the refractive indices of the two media. Fresnel equations mentioned in equations 3.2 to 3.5 are used to determine the fraction of light that is reflected or transmitted [2]. They are derived based on snell's law and boundary conditions of electromagnetic fields. For s-polarized light, electric field vector is perpendicular to the plane of incidence and it

is parallel in the case of p-polarized light. Fresnel reflection and transmission coefficients for s-polarized light are mentioned in equations 3.2 and 3.3:

$$r^s_{1,2} = \frac{n_1 \cos\theta_i - n_2 \cos\theta_t}{n_1 \cos\theta_i + n_2 \cos\theta_t} \tag{3.2}$$

$$t^s_{1,2} = \frac{2n_1 \cos\theta_i}{n_1 \cos\theta_i + n_2 \cos\theta_t} \tag{3.3}$$

For p-polarized light fresnel equations are mentioned in equations 3.4 and 3.5:

$$r^p_{1,2} = \frac{n_1 \cos\theta_t - n_2 \cos\theta_i}{n_1 \cos\theta_t + n_2 \cos\theta_i} \tag{3.4}$$

$$t^p_{1,2} = \frac{2n_1 \cos\theta_i}{n_1 \cos\theta_t + n_2 \cos\theta_i} \tag{3.5}$$

$r^s_{1,2}$ and $t^s_{1,2}$ are reflection and transmission coefficients for a s-polarized wave incident of interface of medium 1 and medium 2, respectively. $r^p_{1,2}$ and $t^p_{1,2}$ are reflection and transmission coefficients for a p-polarized wave, respectively.

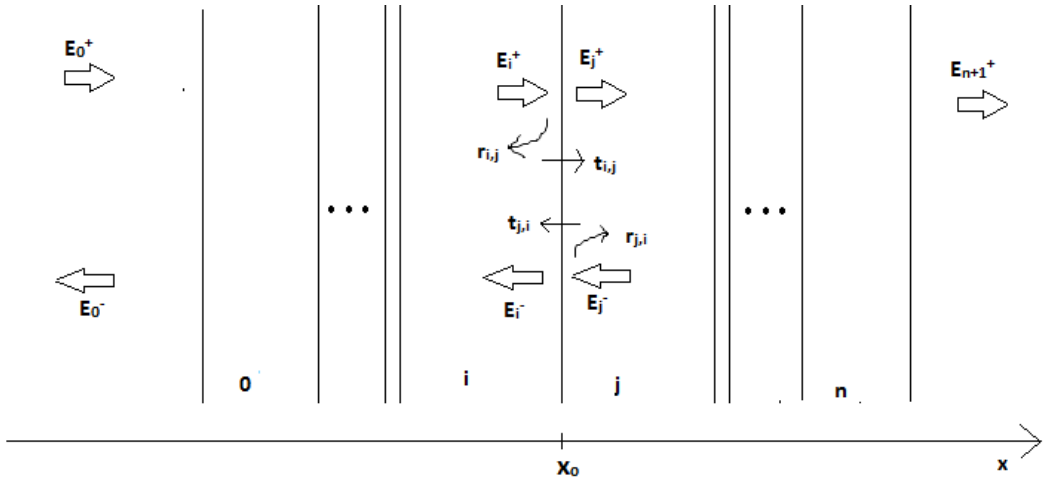

Figure 3.3: Sketch of n-layer device showing interface of layer i and j for calculation of interface matrix

In the Figure 3.3, E_0^+ and E_0^- are incident and reflected electric field components of the light. E_i^+ and E_i^- indicate the incident and reflected electric field of i^{th} layer respectively. E_{n+1}^+ is the transmitted component of electric field from the overall device. '+' and '-' superscripts demonstrate propagation in the forward and backward directions respectively. The backward component is due to reflection at the interface between two media. At any point in the device, total electric field is due to combination of forward and backward propagating. By considering the

interface between layer i and layer j, equation 3.6 can be obtained from transmitted component of $E_i^+(x_0)$ and reflected component of $E_j^-(x_0)$. Similarly, equation 3.7 can be obtained from reflected component of $E_i^+(x_0)$ and transmitted component of $E_j^-(x_0)$

$$\boldsymbol{E_j^+(x_0) = t_{i,j}E_i^+(x_0) + r_{j,i}E_j^-(x_0)} \tag{3.6}$$

$$\boldsymbol{E_i^-(x_0) = r_{i,j}E_i^+(x_0) + t_{j,i}E_j^-(x_0)} \tag{3.7}$$

$t_{i,j}$ and $r_{i,j}$ are transmission and reflection coefficients at the interface when light is travelling from medium i to medium j. For light traveling from j to i, transmission and reflection coefficients are termed as $t_{j,i}$ and $r_{j,i}$, respectively. Reflection and transmission coefficients depend on refractive index and extinction coefficient of the medium as explained in equations 3.2 to 3.5.

By rewriting equations 3.6 and 3.7 and using formulations of $r_{ij} = -r_{ji}$ and $-r_{ij}r_{ji}+t_{ij}t_{ji} = 1$, we can relate the electric fields on the left side of the interface to the fields on the right sides as below:

$$\begin{pmatrix} \boldsymbol{E_i^+(x_0)} \\ \boldsymbol{E_i^-(x_0)} \end{pmatrix} = \begin{pmatrix} \frac{1}{t_{i,j}} & \frac{r_{i,j}}{t_{i,j}} \\ \frac{r_{i,j}}{t_{i,j}} & \frac{1}{t_{i,j}} \end{pmatrix} \begin{pmatrix} \boldsymbol{E_j^+(x_0)} \\ \boldsymbol{E_j^-(x_0)} \end{pmatrix} \tag{3.8}$$

In the equation 3.8, the matrix is termed as 'interface' matrix as it correlates the field components on the both sides of the interface of two layers.

$$\boldsymbol{I_{i,j}} = \begin{pmatrix} \frac{1}{t_{i,j}} & \frac{r_{i,j}}{t_{i,j}} \\ \frac{r_{i,j}}{t_{i,j}} & \frac{1}{t_{i,j}} \end{pmatrix} \tag{3.9}$$

where $\boldsymbol{r_{i,j}} = \frac{\tilde{n}_i - \tilde{n}_j}{\tilde{n}_i + \tilde{n}_j}$, $\boldsymbol{t_{i,j}} = \frac{2\tilde{n}_i}{\tilde{n}_i + \tilde{n}_j}$. These reflection and transmission coefficients for the interface of layer i and j can be obtained from equations 3.2 to 3.5 for normal incidence of light. Polarization of electric field doesn't matter because of normal incidence. Complex refractive index mentioned in equation 3.10 is combination of refractive index (n) and extinction coefficient (k).

$$\boldsymbol{\tilde{n} = n + ik} \tag{3.10}$$

As the wave travels within a layer, there will be phase shift and absorption within the material. The phase shift is governed by the refractive index of the medium and absorption is governed by extinction coefficient as determined by equation 3.12. Layer matrix describes the propagation within the layer [3]. It is used to calculate the electric fields at the left side (E_l^+, E_l^-) of a layer if the fields on the right side (E_r^+, E_r^-) of this layer are known. These electric field components are shown in Figure 3.4. In layer matrices, off-diagonal elements are zeros as the reflection doesn't occur within a layer.

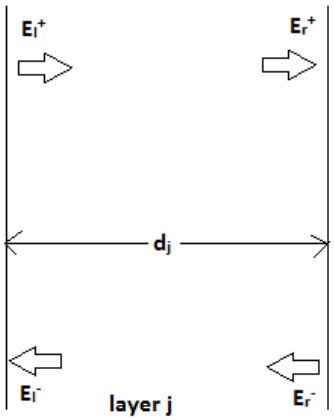

Figure 3.4: Representation of electric components on left (E_l^+, E_l^-) and right (E_r^+, E_r^-) ends of layer j for formulation of layer matrix

$$E_r^+ = e^{i\xi_j d_j} E_l^+$$

$$E_l^- = e^{i\xi_j d_j} E_r^-$$

where $\xi_j = (2\pi/\lambda)\tilde{n}_j$ and d_j is the thickness of layer j.

$$\begin{pmatrix} E_l^+ \\ E_l^- \end{pmatrix} = \begin{pmatrix} e^{-i\xi_j d_j} & 0 \\ 0 & e^{i\xi_j d_j} \end{pmatrix} \begin{pmatrix} E_r^+ \\ E_r^- \end{pmatrix} \tag{3.11}$$

$$Lj = \begin{pmatrix} e^{-i\xi_j d_j} & 0 \\ 0 & e^{i\xi_j d_j} \end{pmatrix} \tag{3.12}$$

In order to calculate device matrix, first we consider a device with two layers as shown in Figure 3.5 and later extended to n-layer device. The electric field components of the overall device can be related by multiplying interface and layer matrices as shown below:

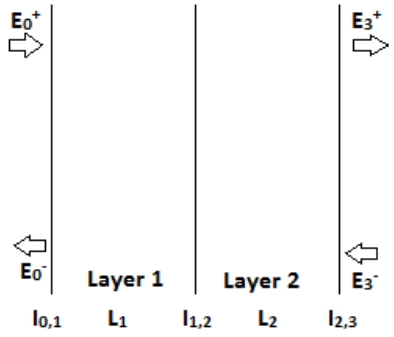

Figure 3.5: Demonstration of two layer device where $I_{0,1}$, $I_{1,2}$ and $I_{2,3}$ are interface matrices and L_1 and L_2 are layer matrices

$$\begin{pmatrix} E_0^+ \\ E_0^- \end{pmatrix} = I_{0,1} L_1 I_{1,2} L_2 I_{2,3} \begin{pmatrix} E_3^+ \\ E_3^- \end{pmatrix}$$

E_0^+ and E_0^- are electric field components on the left side of layer 1 of device shown in Figure 3.5. E_3^+ and E_3^- are electric field components on the right side of final layer 2. These components of the device can be related by multiplication of all the interface matrices ($I_{0,1}$, $I_{1,2}$ and $I_{2,3}$) and the layer matrices (L_1 and L_2) of the device.

Similarly, the device matrix of n-layer device can be obtained by multiplying all interface matrices and layer matrices and can be represented as below [4]:

$$\begin{pmatrix} E_0^+ \\ E_0^- \end{pmatrix} = I_{0,1} \prod_{i=1}^{i=n} L_i I_{i,i+1} \begin{pmatrix} E_{n+1}^+ \\ E_{n+1}^- \end{pmatrix} \tag{3.13}$$

$$S = \begin{pmatrix} S_{11} & S_{12} \\ S_{21} & S_{22} \end{pmatrix} = I_{0,1} \prod_{i=1}^{i=n} L_i I_{i,i+1} \tag{3.14}$$

This device matrix or scattering matrix (S) relates the electric fields left and right ends of the entire multi-layer device. From this matrix, reflection and transmission coefficients of the device are as below.

$$r = \frac{E_0^-}{E_0^+} = \frac{S_{21}}{S_{11}} \tag{3.15}$$

$$t = \frac{E_{n+1}^+}{E_0^+} = \frac{1}{S_{11}} \tag{3.16}$$

r and t are reflection and transmission coefficients of the device. E_0^+, E_0^- and E_{n+1}^+ are incident, reflected and transmitted electric field components of the device. Equation 3.15 is calculation of reflection coefficient of the device, which is the ratio

of the reflected (E_0^-) to the incident (E_0^+) electric field components of the device. Equation 3.16 is calculation of transmission coefficient of the device, which is the ratio of the transmitted (E_{n+1}^+) to the incident (E_0^+) electric field components of the device.

3.1.2 Electric field

Interface matrix, layer matrix, reflection coefficient and transmission coefficient are determined according to equations 3.9, 3.11, 3.15 and 3.16, respectively. By using these equations, electric field within a layer at a distance x from the interface of layer j-1 and j is calculated in the following manner. The layers from 0 to j-1 are denoted as stack f and from j+1 to n as stack b. Here t_f and r_f are transmission and reflection coefficients of stack f, respectively. r_b is the reflection coefficients of stack b. $E_j^+(x)$ is the forward electric field component at a distance x in the layer j as shown in Figure 3.6. It is combination of components E_{j1}, E_{j2}, E_{j3} and so on as shown in equation 3.17:

$$E_{j1} = E_0^+ t_f e^{i\xi_j x}$$

E_{j1} is the transmitted component of E_0^+ through the stack f into the layer j and after travelling distance x within the layer j.

$$E_{j2} = E_0^+ t_f e^{i\xi_j x} e^{i\xi_j (d_j - x)} r_b e^{i\xi_j d_j} r_f e^{i\xi_j x}$$

$$E_{j2} = E_0^+ t_f e^{i\xi_j x} r_b r_f e^{2i\xi_j d_j}$$

$$E_{j2} = E_{j1} r_b r_f e^{2i\xi_j d_j}$$

E_{j2} is the doubly reflected component of E_{j1} within the layer j from the stack b (r_b) and then stack f (r_f).

$$E_{j3} = E_0^+ t_f e^{i\xi_j x} (r_b r_f e^{2i\xi_j d_j})^2$$

$$E_{j3} = E_{j2} r_b r_f e^{2i\xi_j d_j}$$

E_{j3} is the doubly reflected component of E_{j2} within the layer j from the stack b (r_b) and then stack f (r_f).

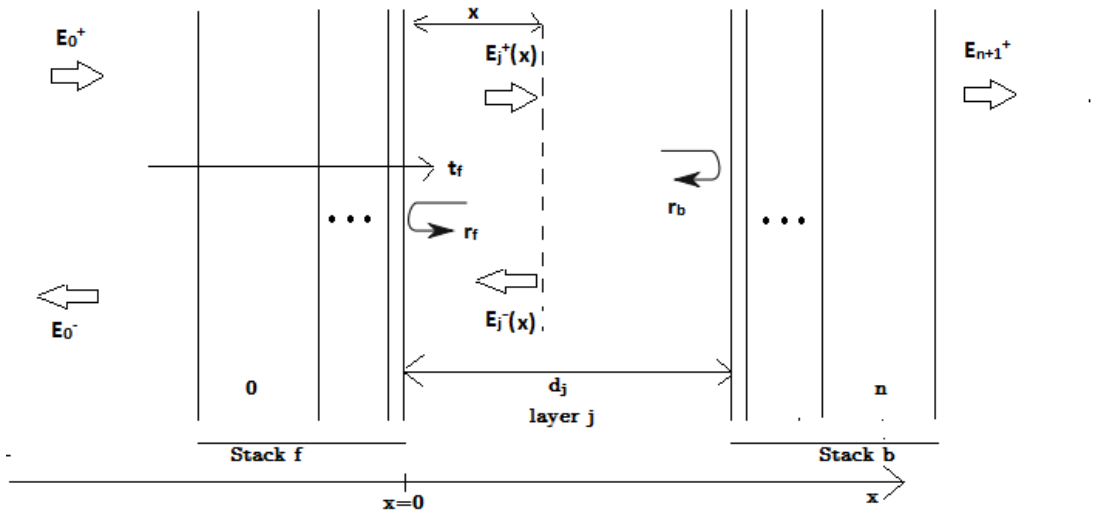

Figure 3.6: Exemplification for derivation of electric field distribution within a layer j. All layers to the left of layer j is considered as stack f and to the right of layer j as stack b.

By considering E_{j1}, E_{j2}, E_{j3} and so on, we can write total $E_j^+(x)$ as below:

$$E_j^+(x) = E_{j1} + E_{j2} + E_{j3} + \ldots \tag{3.17}$$

$$= \frac{E_0^+ t_f e^{i\xi_j x}}{1 - r_b r_f e^{2i\xi_j d_j}} \tag{3.18}$$

The backward electric field component ($E_j^-(x)$) can be obtained from equation 3.18 by including the reflection from stack b (r_b) and the phase change component $e^{2i\xi_j(d_j - x)}$ which tells about the phase shift and absorption of the electric field component for travelling a distance of $2(d_j\text{-}x)$ within the layer j:

$$E_j^-(x) = E_j^+(x)\, r_b\, e^{2i\xi_j(d_j - x)} \tag{3.19}$$

Electric field within a layer at a distance x ($E_j(x)$) is obtained by summation of equation of 3.18 and equation 3.19:

$$E_j(x) = E_j^+(x) + E_j^-(x) = \frac{E_0^+ t_f}{1 - r_b \check{r}_f e^{2i\xi_j d_j}} (e^{i\xi_j x} + r_b e^{i\xi_j(2d_j - x)}) \tag{3.20}$$

Electric field within the layer at x=0 can be obtained from equation 3.20 by putting x =0:

$$E_j(0) = \frac{E_0^+ t_f}{1 - r_b \check{r}_f e^{2i\xi_j d_j}} (1 + r_b e^{i\xi_j 2d_j}) \tag{3.21}$$

3.1.3 Reflectance

Reflectance is measured from the reflection coefficient which is the ratio of reflected to incident electric field components. Reflectance of the device is defined as square of the reflection coefficient [5] as shown in equation 3.22. The reflectance spectrum is the plot of the reflectance as a function of wavelength. From the device matrix (S), reflection coefficient (r) of the device can be found as shown in equation.

$$\boldsymbol{R = |r|^2} \tag{3.22}$$

3.1.4 Optical power dissipation

It is the time-averaged energy dissipation or absorbed power in different layers of the device. The optical power dissipation [6] as a function of distance can be calculated using optical electrical field which is obtained from equation 3.20. The formulation for optical power dissipation is [7]:

$$\boldsymbol{Q(x) = \frac{1}{2} c\epsilon_0 \alpha n |E(x)^2|} \tag{3.23}$$

Where c is the speed of light is (3×10^8 m/s), ϵ_0 is permittivity of vacuum (8.85×10^{-12} F/m), n is the real index of refraction, α is the absorption coefficient ($\alpha = 4\pi k / \lambda$), λ is the vacuum wavelength and E(x) is the total electrical optical field at the point x. For a plane electromagnetic wave, intensity and electric field are related by:

$$\boldsymbol{I = \frac{1}{2} c\epsilon_0 E^2}$$

As the wave travels inside a medium, refractive index of the medium needs to be considered for calculation of speed. By considering absorption coefficient (α), optical power dissipation in equation 3.23 can be obtained by $Q = \alpha I$.

This optical power dissipation can be measured for a particular wavelength or for whole spectrum of wavelengths in consideration. In this thesis, we focused on the measurement over whole spectrum.

3.1.5 Absorptance

It is the ratio of power absorbed by the device to that incident upon it. The absorptance gives wavelength-dependent absorbed power in different layers of the device. From the modeling, the absorptance gives absorbed power for each wavelength of the wavelength spectrum under consideration [8].

$$\boldsymbol{A_j = \frac{1}{S_0} \int_{d_{j-1}}^{d_j} Q_j(x)\, dx} \tag{3.24}$$

where S_0 is the irradiance from air. $Q_j(x)$ is obtained from equation 3.23.

Power re-distribution model describes the distribution of the optical power dissipation, for the different layers as well as for different wavelengths.

In MATLAB, thickness, refractive index and extinction coefficient are the parameters considered for each layer. Interface and layer matrices are calculated for each wavelength. Device matrix and electric field within the layer were measured using the interface and layer matrices.

3.2 Device fabrication

ITO substrates were cleaned in ultrasonic bath in acetone, isopropanol and de-ionized water sequentially for 5 minutes each [9]. Cleaned ITO substrates were treated with UV ozone plasma for 5 minutes. Cleaned ITO substrates were loaded in the chamber of thermal evaporator for deposition of layers of organic solar cell.

For the purpose of anode interfacial layer, vandium oxide (V_2O_5) or 4,4',4''- Tris[(3-methylphenyl) -phenylamino]triphenylamine (m-MTDATA) were used in this experiment. V_2O_5 is an inorganic material and m-MTDATA is an organic material. As of donor and acceptor layers, copper phthalocyanine (CuPc) and buckminsterfullerene (C_{60}) were used, respectively. For the purpose of cathode interfacial layer, tris(8-hydroxyquinolinato)aluminium (Alq_3) was used. m-MTDATA, CuPc, C_{60} and Alq_3 are small molecule type organic materials. aluminum (Al) was used as cathode for the device. All materials including ITO coated glass substrates were purchased from sigma-aldrich. No further purification

was performed for any of the materials. For deposition of all these materials thermal evaporation method was used.

3.2.1 Thermal evaporation

Thermal evaporation is done by resistive heating of materials [10]. A thermal evaporator consists of boat, crucible, shutter, substrate holder and thickness monitor as shown in Figure 3.7. The source material to be evaporated is placed in the crucible or directly in the boat. The substrate holder which holds the substrates is placed above the source at fixed distance. The source to substrate distance was 21 cm in this experiment. Molecules or atoms from source to substrate are transformed in a controlled manner by adequate base pressure, voltage and current. Roughing pump and diffusion pumps are present along with the thermal evaporator for vacuum. The source is heated till the material is sublimed. Quartz crucible was used in deposition of all materials. The boat is a wire-basket type and made of tungsten. After the loading the substrates and source material, glass jar was used to seal the chamber. After adequate vacuum of $4x10^{-6}$ mbar was obtained, voltage is raised in steps according to sublimation temperature of the source material. By application of voltage, electrical energy is converted into heat energy in the boat. Upon achieving desired evaporation rate, the substrate shutter will be opened which will be closed after deposition of required thickness. Thickness monitor based on quartz crystal records the deposited thickness.

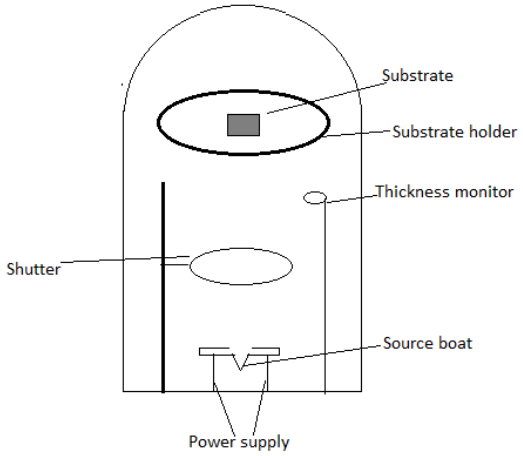

Figure 3.7: Schematic of thermal evaporator

3.2.2 Fabrication procedure

The devices are made on Indium Tin Oxide (ITO) coated glass substrate. On top of cleaned ITO substrate, anode interfacial layer is deposited. For active layer of organic solar cell, donor and acceptor layers are deposited sequentially to obtain single heterojunction organic solar cells. Later, cathode interfacial layer is deposited over the acceptor layer and finally cathode is deposited. For the reference sample, AIL is not deposited.

3.3 Characterization

3.3.1 Current-voltage characteristics

The current-voltage characteristics of fabricated solar cells were measured in dark and light conditions. The anode of the organic solar cells is connected to positive terminal and cathode of the device is connected to negative terminal of DC probe station. The voltage is swept from -0.2V to +2V using source meter and corresponding current values are recorded. Similar measurement is taken under solar simulation using solar simulator for J-V characteristics under light conditions. Sol3A Class AAA Solar Simulator was used to obtain light of desired intensities.

3.3.2 Thickness and refractive index

Ellipsometry is used to measure the thickness, refractive index and extinction coefficient of every material. Reflection or transmission of light from a sample leads to change in polarization.

The primary tools for collecting ellipsometry data include the following: light source, polarization generator, sample, polarization analyzer, and detector. Polarized light is reflected or transmitted from the sample and the output polarization is measured (Figure 3.8). Electric fields parallel and perpendicular to the plane of incidence are considered p- and s- polarized, respectively. Ellipsometry measures how p- and s- components change upon reflection or transmission.

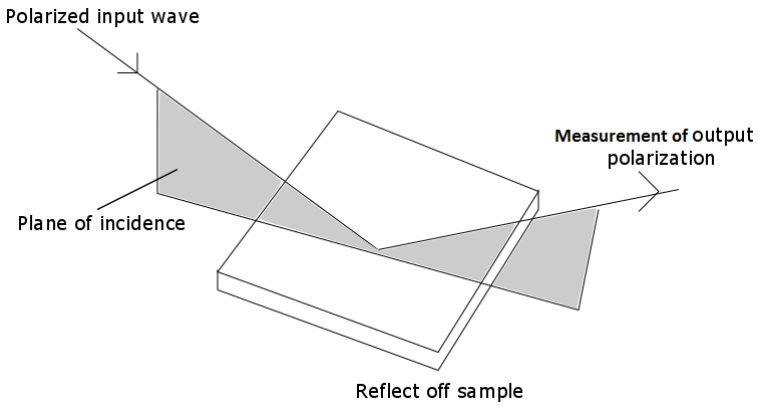

Figure 3.8: A typical ellipsometry configuration, where polarized input wave is reflected from the sample surface and change in polarization is measured

The change in polarization is measured as:

$$\rho = \tan(\psi)e^{i\Delta} \tag{3.25}$$

Where ψ is the amplitude ratio and Δ is the phase difference.

We used J.A.Woollam M2000U ellipsometer for measurement of thickness, refractive index and extinction coefficient of all the materials of organic solar cell.

3.3.3 Reflectance measurement

Spectrophotometry is a method to measure percentage of reflected or transmitted or absorbed the light by measuring the intensity of light. Spectrophotometers can be classified into two classes based on nature of beam: single beam and double beam. In single beam spectrophotometers, entire light without splitting passes through the sample. In double beam spectrophotometers the light source is split into two separate beams before reaching the sample. One beam passes through the sample and the second one through the reference sample. For reflectance measurements, spectrophotometer compares the amount of light reflecting from the test and reference sample.

A spectrophotometer consists [11] of a light source, a collimator, a monochromator, a wavelength selector, a cuvette for sample and a photoelectric detector as illustrated in Figure 3.9. The collimator (lens) transmits a straight beam of light that passes through a monochromator (prism) to split it into different wavelengths

(spectrum). Then a wavelength selector (slit) transmits only the selected wavelengths which travel through the sample and the photometer detects the transmitted intensity of light.

Initially, the measurement of intensity of the light beam, I_0, is measured without the sample. Then the sample is set in the path of the measurement light beam, and the intensity of the light beam after it passes through the sample, I_t, is measured.

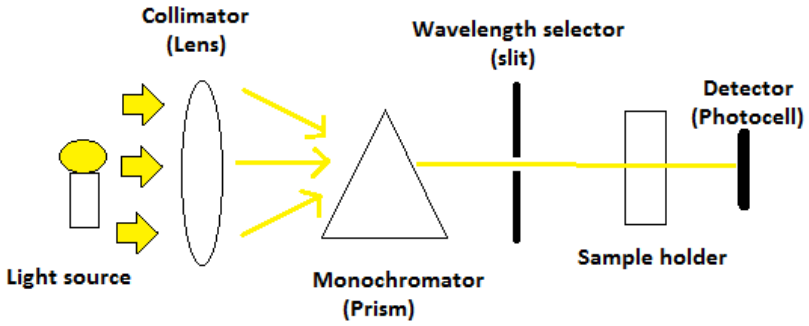

Figure 3.9: Illustration of working principle of a spectrophometer

The transmittance can be measured by the following equation:

$$\boldsymbol{T = \frac{I_t}{I_0}} \tag{3.26}$$

The absorbance can be measured by the following equation using measured transmittance:

$$\boldsymbol{A = \log_{10}\frac{1}{T}} \tag{3.27}$$

We used Shimadzu MPC3600 UV-VIS-NIR spectrophotometer for measurement of reflectance of fabricated organic solar cells.

References

[1] L. A. A. Pettersson, L. S. Roman, and O. Inganäs, "Modeling photocurrent action spectra of photovoltaic devices based on organic thin films," *J. Appl. Phys.*, 86(1999), pp. 487–496.

[2] P. Taylor, A. I. Lvovsky, and A. I. Lvovsky, "Fresnel Equations," *Encycl.*

Opt. Eng., 2013.

[3] P. Peumans, A. Yakimov, and S. R. Forrest, "Small molecular weight organic thin-film photodetectors and solar cells," *J. Appl. Phys.*, 93(2003), pp. 3693–3723.

[4] D. W. Sievers, V. Shrotriya, and Y. Yang, "Modeling optical effects and thickness dependent current in polymer bulk-heterojunction solar cells," *J. Appl. Phys.*, 100(2006).

[5] W. Tress, *Organic solar cells: Theory, Experiment and Device Simulation*.

[6] H. R. Barry P.Rand, *Organic Solar Cells: Fundamentals, Devices, and Upscaling*.

[7] A. J. Moulé, J. B. Bonekamp, and K. Meerholz, "The effect of active layer thickness and composition on the performance of bulk-heterojunction solar cells," *J. Appl. Phys.*, 100(2006), p. 94503.

[8] N. K. Persson, H. Arwin, and O. Inganas, "Optical optimization of polyfluorene-fullerene blend photodiodes," *J. Appl. Phys.*, 97(2005).

[9] J.-H. J. Kim, S.-Y. S. Jung, and I. I.-K. Jeong, "Optical modeling for polarization-dependent optical power dissipation of thin-film organic solar cells at oblique incidence," *J. Opt. Soc. Korea*, 16(2012), pp. 6–12.

[10] P. Huang, C. Huang, K. Chen, J. Ke, Y. Wang, and C. Kang, "Improved Reliability of Small Molecule Organic Solar Cells by Double Anode Buffer Layers," 2014.

[11] Norm Hardy, "What is Thin Film Deposition By Thermal Evaporation?" [Online]. Available: http://www.semicore.com/news/71-thin-film-deposition-thermal-evaporation. [Accessed: 19-Nov-2017].

[12] F. M. Sanda, M. E. Victor, T. A. Monica, and C. Alina, "Spectrophotometric Measurements Techniques Fermentation Process (Part One): Base Theory

for Uv-Vis Spectrophotometric Measurements," *Hungary-Romania Cross-Border Co-operation Program.*, 2012.

Chapter 4

Anode interfacial layer of small molecule organic solar cells

The influence of anode interfacial layer on the performance of a CuPc:C60 based small molecule organic solar cell was analyzed. The procedure of fabricated device is explained in section 4.1. The results obtained from the modeling and the characterizations are presented in section 4.2. Section 4.3 discusses the conclusions from the modeling and characterization results.

4.1 Devices

The schematic of device investigated is shown in Figure 4.1. ITO and Al are anode and cathode, respectively. Alq_3 was used as cathode interfacial layer. For donor and acceptor, CuPc and C_{60} materials were used, respectively. AIL was made either of Vanadium oxide (V_2O_5) and 4,4',4''-Tris[(3-methylphenyl)-phenylamino]triphenylamine (m-MTDATA). Two thicknesses of AIL were considered: 5 nm and 10 nm. The optical electrical field intensity, device reflectance, power dissipation, absorptance and power redistribution measurements were done using transfer matrix approach as explained in section 3.1.1. Modeling and simulation were done using MATLAB. For device fabrication, thermal evaporator was used for deposition of all materials such as V_2O_5, m-MTDATA, CuPc, C_{60}, Alq_3 and Al. All materials were deposited under pressure conditions of $4x10^{-6}$ mbar and deposition rates of 1-2 Å/s. Thickness was confirmed by ellipsometer. For characterization part, current density-voltage (J-V) characteristics were measured using solar simulator with source meter, while reflectance was

measured using spectrophotometer. Fabrication and characterization was carried out in Centre for Nano Science and Engineering (CeNSE), Indian Institute of Science (IISc), Bangalore under Indian Nanoelectronics Users Program (INUP).

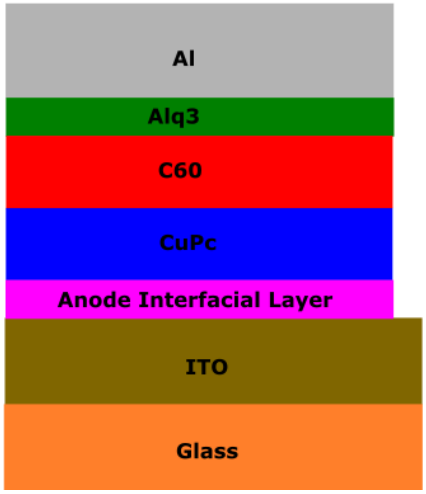

Figure 4.1: Schematic of the device. Here, anode interfacial layer is V_2O_5 or m-MTDATA with thickness 5 nm or 10 nm

4.2 Results

This section presents the results obtained from modeling using transfer matrix approach and measurement of fabricated devices.

4.2.1 Optical electric field

Refractive index (n) and extinction coefficient (k) were extracted from ellipsometry. They were used in calculation of optical electric field intensity, device reflectance, power dissipation, absorptance and power redistribution, using transfer matrix method. Thickness of layers were: ITO(150 nm)/AIL/CuPc(40 nm)/C_{60}(40 nm)/Alq_3(9 nm)/Al(120 nm).

Figure 4.2 (a) is the electric field distribution of device with V_2O_5 of 5 nm thickness. It was observed the electric field intensity peak lies within the active layer, which is a desired requirement for maximizing efficiency of the device. In the case of 10 nm thickness, as shown in Figure 4.2 (b), electric field intensity peak lies within the active layer but the peak value decrease by 0.6%.

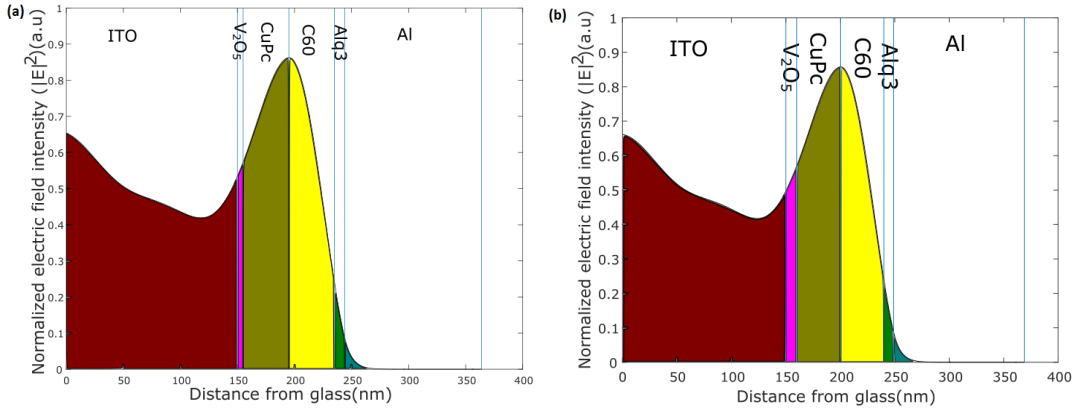

Figure 4.2: Optical electric field intensity distribution of device with V_2O_5 as AIL of (a) 5 nm and (b) 10 nm thickness

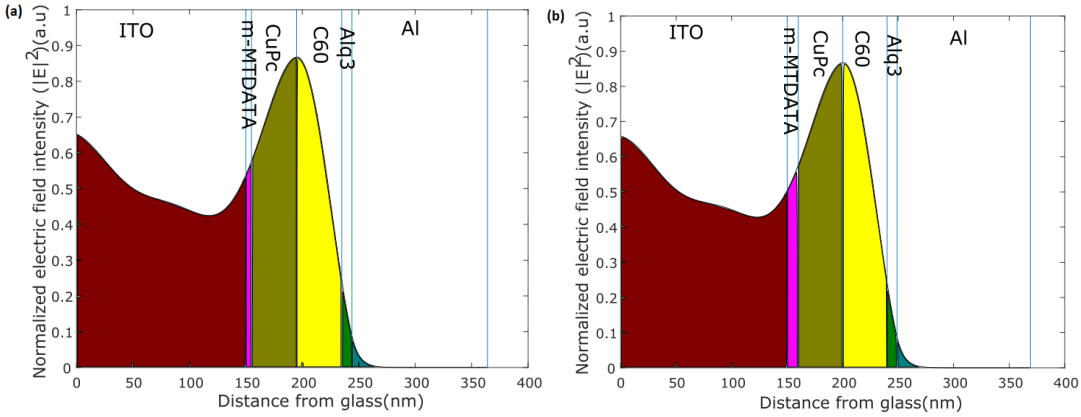

Figure 4.3: Optical electric field intensity distribution of device with m-MTDATA as AIL of (a) 5 nm and (b) 10 nm thickness

Figure 4.3 (a) and (b) are electric field distribution of device with m-MTDATA of 5 nm and 10 nm thickness, respectively. For the device with 5 nm thickness of m-MTDATA as AIL, electric field intensity peak was higher by 0.57% compared to device with V_2O_5 of 5 nm. The peak value with 5 nm and 10 nm of m-MTDATA remains the same. The peak value of device with 10 nm thickness of m-MTDATA as AIL was higher by 1.17% compared to device with 10 nm V_2O_5.

4.2.2 Device reflectance

Figure 4.4 (a) and (b) are reflectance of the device with V_2O_5 of 5 nm and 10 nm, respectively. In both cases, it was observed that peak reflectance was around 550 nm. The peak reflectance of device with V_2O_5 of 10 nm was higher by 2.54% when compared with device of V_2O_5 of 5 nm.

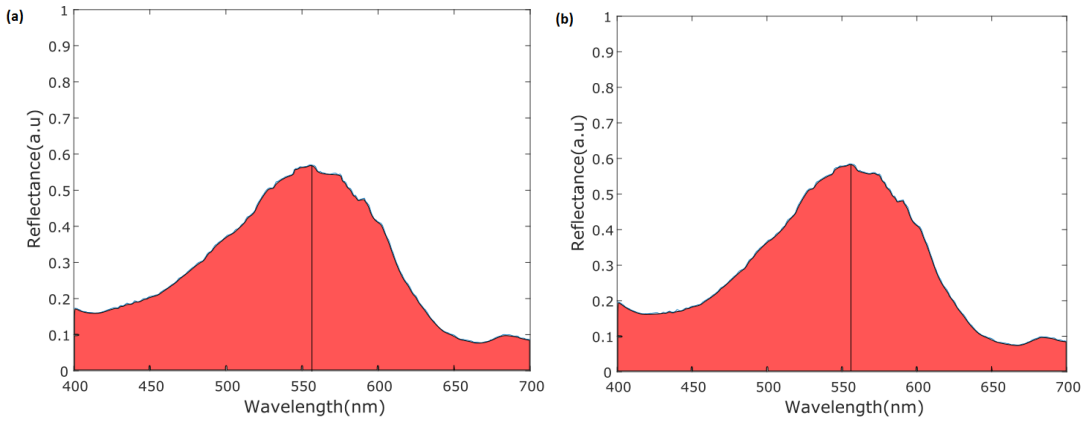

Figure 4.4: Reflectance of the device with V_2O_5 of (a) 5 nm and (b) 10 nm

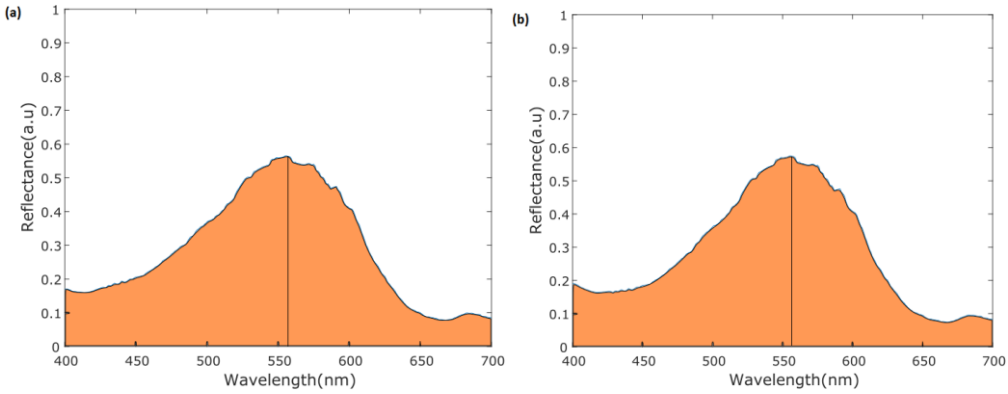

Figure 4.5: Reflectance of the device with m-MTDATA as AIL of (a) 5 nm and (b) 10 nm

Figure 4.5 (a) and (b) are reflectance of the device with m-MTDATA of 5 nm and 10 nm thickness, respectively. It was observed that peak reflectance of device with m-MTDATA of 5 nm was lower by 0.93% compared to device with V_2O_5 of 5 nm. For device with m-MTDATA of 10 nm thickness, peak reflectance was lower by 1.74% compared to device with V_2O_5 of 10 nm. As reflectance of the device is ratio of reflected and incident electric field components, it can be said that the reflected electric field component of the device increased with increase in thickness of AIL.

4.2.3 Power dissipation

Figure 4.6 (a) and (b) are power dissipation distribution of devices with V_2O_5 of 5 nm and 10 nm thickness, respectively. It was observed that maximum power dissipation is confined within the active layer materials of CuPc and C_{60}. Peak of power dissipation within the CuPc and C60 layers is near to CuPc:C_{60} interface, which is a desired requirement for maximization of efficiency of the device.

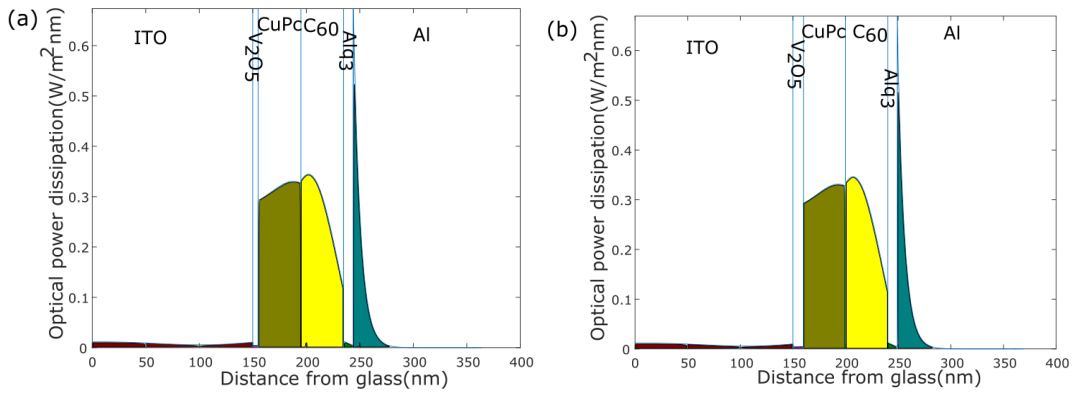

Figure 4.6: Optical power dissipation of device with V_2O_5 as AIL of (a) 5 nm and (b) 10 nm

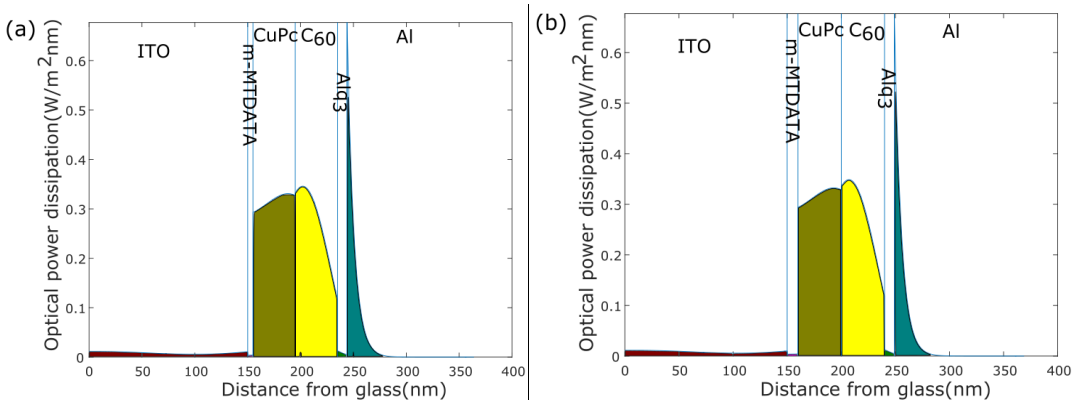

Figure 4.7: Optical power dissipation of the device with m-MTDATA as AIL of (a) 5 nm and (b) 10 nm

Figure 4.7 (a) and (b) are power dissipation distribution of devices with m-MTDATA of 5 nm and 10 nm thickness, respectively. In case of devices with m-MTDATA as AIL, higher power dissipation was observed in the active layer compared V_2O_5 as AIL. Power dissipation depends on the absorption coefficient of the material. Due to low absorption coefficient of ITO material, lower power dissipation was observed in the ITO layer when compared to CuPc and C_{60} materials. For aluminum layer, due to high absorption coefficient higher power dissipation was observed near the interface of Alq_3 and Al layer.

4.2.4 Absorptance

Figure 4.8 (a) and (b) are absorptance of all layers of device with V_2O_5 of 5 nm and 10 nm thickness as AIL, respectively. Absorptance tells about the power dissipation within a layer for each wavelength. From the absorptance curves, it was observed

that CuPc material is absorbing wavelengths in the range of 550 to 700 nm and C_{60} material is absorbing wavelengths in the range of 400 to 550 nm.

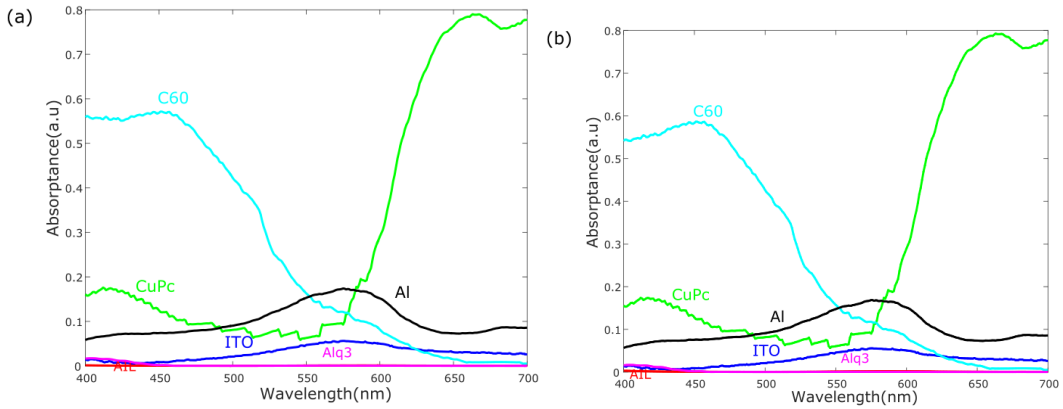

Figure 4.8: Absorptance of various layers of device with V_2O_5 as AIL of (a) 5 nm and (b) 10 nm

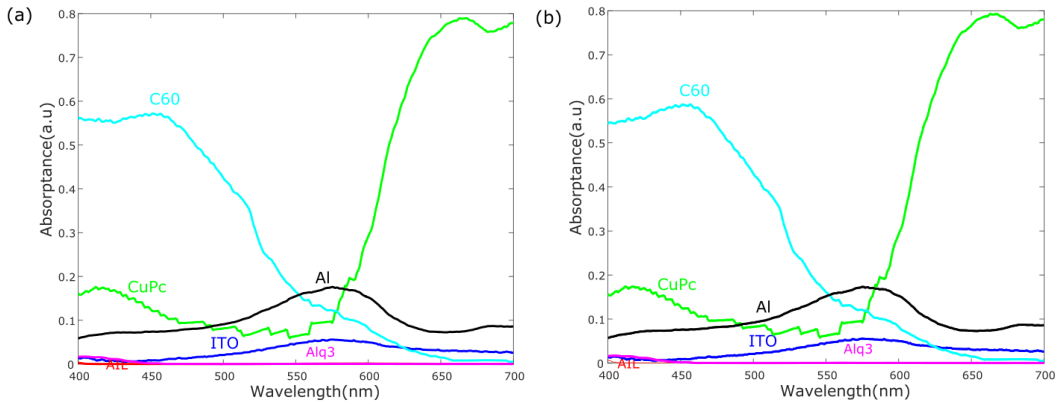

Figure 4.9: Absorptance of various layers of device with m-MTDATA as AIL of (a) 5 nm and (b) 10 nm.

Figure 4.9 (a) and (b) are absorptance of various layers of device with m-MTDATA of 5 nm and 10 nm thickness as AIL. The absorptance of active layers is higher in case of devices with m-MTDATA as AIL when compared to devices with V_2O_5 as AIL. It was observed that absorption is higher in aluminum layer for wavelengths near 560 nm.

4.2.5 Power redistribution

Figure 4.10 (a) and (b) are power redistribution of device with V_2O_5 of 5 nm and 10 nm thickness, respectively. Power redistribution curves shows how incoming energy is shared across different layers of the device as a function of wavelength. It was

observed that CuPc layer is sharing higher wavelengths and C_{60} layer is sharing the lower wavelengths of incoming energy.

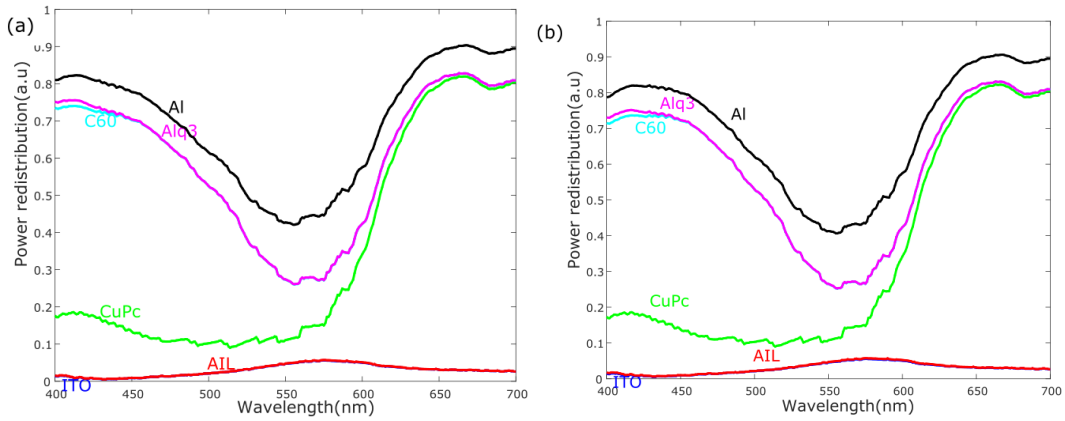

Figure 4.10: Power redistribution of device with V_2O_5 as AIL of (a) 5 nm and (b) 10 nm.

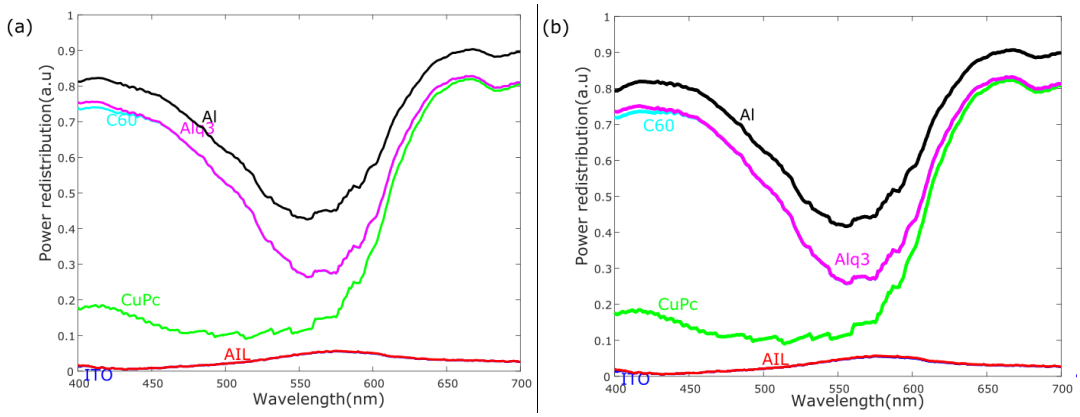

Figure 4.11: Power redistribution of device with m-MTDATA as AIL of (a) 5 nm and (b) 10 nm.

Figure 4.11 (a) and (b) are power redistribution of device with m-MTDATA of 5 nm and 10 nm thickness, respectively. Higher absorption in the active layer materials was observed in devices with m-MTDATA as AIL when compared devices with V_2O_5 as AIL. From power re-distribution curves, the remaining part above aluminum layer can be considered as reflectance of the device.

4.2.6 Electrical characterization

Figure 4.12 (a) and (b) presents J-V characteristics under dark and light conditions for the device with V_2O_5 of 5 nm and 10 nm thickness as AIL. It was observed current density was lower for devices with V_2O_5 of 10 nm thickness compared to devices with 5 nm.

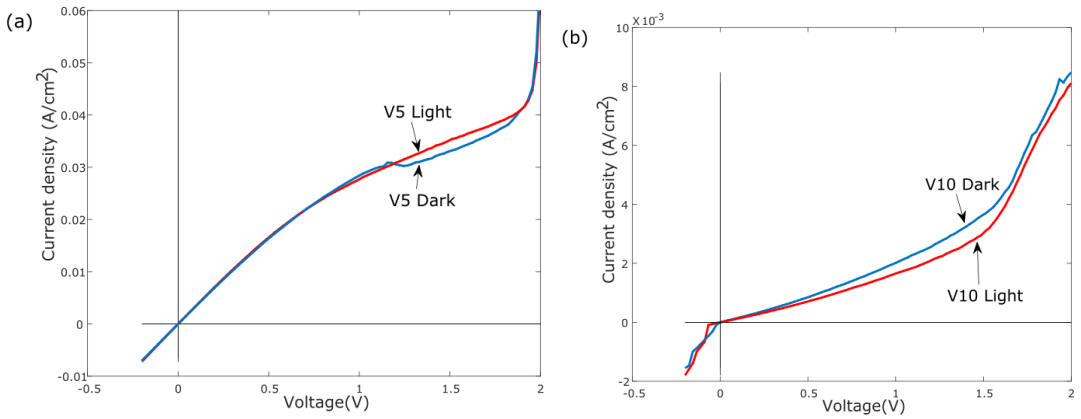

Figure 4.12: J-V characteristics of device with V_2O_5 as AIL of (a) 5 nm and (b) 10 nm thickness. Dark (blue line) and AM1.5 solar simulation (red line)

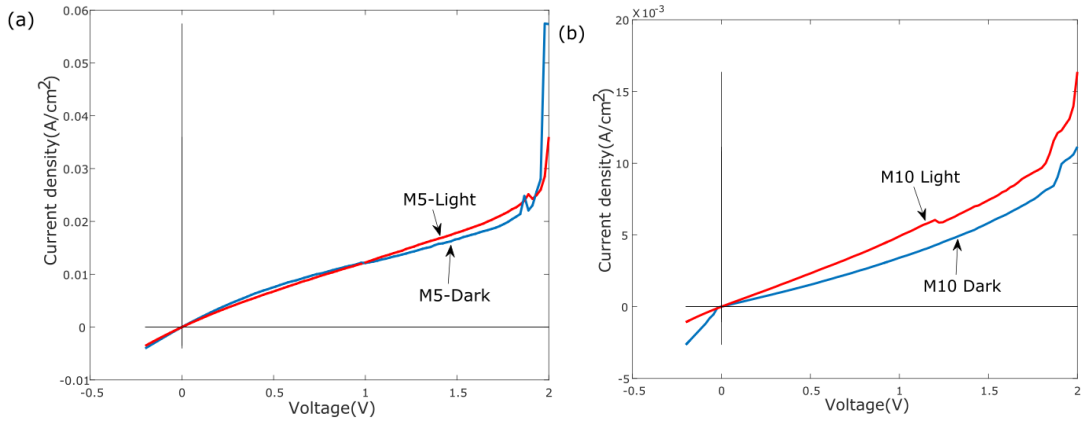

Figure 4.13: J-V characteristics of device with m-MTDATA as AIL of (a) 5 nm and (b) 10 nm thickness. Dark (blue line) and AM1.5 solar simulation (red line)

Figure 4.13 (a) and (b) shows J-V characteristics of the device under dark and light conditions with m-MTDATA of 5 nm and 10 nm thickness as AIL. It was observed lower values of current density compared to device with 5 nm V_2O_5. It was observed that current density values were lower for devices with m-MTDATA of 10 nm thickness but higher than that of device with V_2O_5 of 10 nm thickness.

4.2.7 Optical characterization

Spectrophotometry was done to calculate reflectance of the fabricated devices. The results are presented in the following figures.

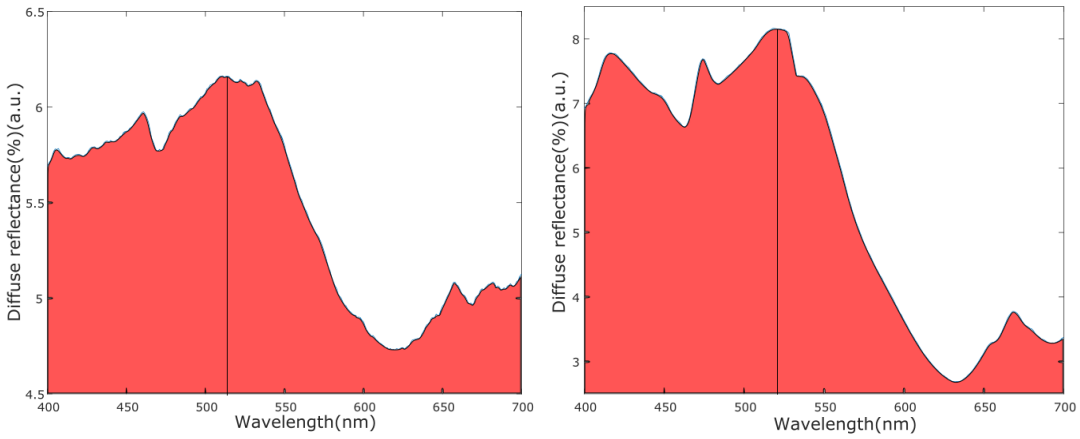

Figure 4.14: Diffuse reflectance (spectrophotometry) of device with V_2O_5 as AIL of (a) 5 nm and (b) 10 nm.

Figure 4.14 (a) and (b) are the reflectance of device with V_2O_5 of 5 nm and 10 nm thickness as AIL. In both cases, the peak reflectance was around 520 nm. It was observed that peak reflectance was higher for device with 10 nm thickness compared to device with V_2O_5 of 5 nm.

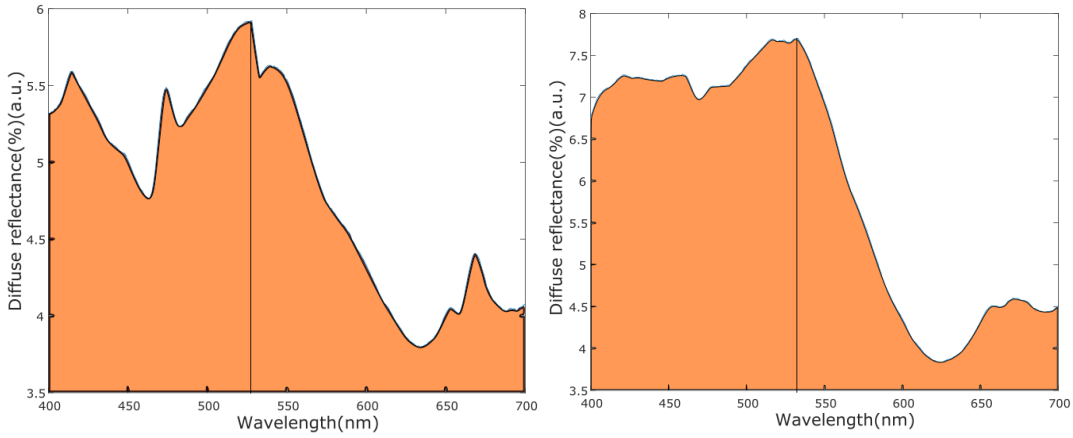

Figure 4.15: Diffuse reflectance (spectrophotometry) of device with m-MTDATA as AIL of (a) 5 nm and (b) 10 nm.

Figure 4.15 (a) and (b) are the reflectance of device with m-MTDATA of 5 nm and 10 nm thickness, respectively. In both cases, it was observed that peak reflectance was around 530 nm. The peak reflectance of the device with m-MTDATA of 5 nm thickness as AIL was lower than the device with V_2O_5 of 5 nm. The peak reflectance of the device with m-MTDATA 10 nm was higher than the device with m-MTDATA of 5 nm.

4.3 Conclusions

From the optical electric field intensity measurements, it was observed that peak of electric field intensity is decreasing with increase in thickness of AIL of V_2O_5 or m-MTDATA. Higher peak electric field intensity was observed in devices with m-MTDATA as AIL compared to devices with V_2O_5. From the device reflectance measured from modeling, higher peak reflectance was observed with increase in thickness of AIL of V_2O_5 or m-MTDATA. The peak reflectance of the device with m-MTDATA as AIL is lower than devices with V_2O_5 as AIL. This trend of reflectance peak of devices measured from modeling was correlated with the reflectance measurement of fabricated devices. The peak reflectance of device measured from modeling was around 550 nm, whereas peak reflectance of fabricated devices was around 520 nm and 530 nm in case in V_2O_5 and m-MTDATA as AIL respectively. From power dissipation measurements, it was known that the maximum power dissipation was confined within the active layer. From the absorptance measurements, CuPc shown absorptance of higher wavelengths and C_{60} shown absorptance of lower wavelengths.

From the current density-voltage characterization, it was observed that with increase in thickness of anode interfacial layer (AIL), lower current density values were obtained. This was observed for both V_2O_5 and m-MTDATA as AIL. For devices with 5nm thickness of AIL, higher current density values were obtained with V_2O_5 compared to m-MTDATA. For devices with 10nm thickness of anode interfacial layer, higher current values were obtained with m-MTDATA compared to V_2O_5.

The device area used in this experiment was small (0.4 cm^2). The mask used for deposition of cathode and other layers was same. Different masks were implemented in the next experiment to avoid short circuit between cathode and anode.

Chapter 5

Cathode interfacial layer of small molecule organic solar cells

In this chapter, the influence of cathode interfacial layer on the performance of a small molecule organic solar cell with CuPc and C_{60} as active layer materials was analyzed. Section 5.1 discusses the fabrication procedure of devices. Section 5.2 presents the results obtained from the modeling and the characterizations. The conclusions from the modeling and characterization are explained in section 5.3.

5.1 Devices

The schematic of the device is shown Figure 5.1. ITO and Al are anode and cathode, respectively. For donor and acceptor, CuPc and C_{60} materials were used, respectively. Anode interfacial layer (AIL) was made either of Vanadium oxide (V_2O_5) and 4,4',4''-Tris[(3-methylphenyl)-phenylamino]triphenylamine (m-MTDATA). Based on analysis of influence of anode interfacial layer in the previous experiment, 5 nm thickness AIL was considered. Cathode interfacial layer (CIL) is made of Alq_3 material and two thicknesses were used: 5 nm and 10 nm. The optical electrical field intensity, device reflectance, power dissipation, absorptance and power redistribution measurements were done using transfer matrix approach as explained in section 3.1.1. Modeling and simulation were done using MATLAB. For device fabrication, thermal evaporator was used for deposition of all materials such as V_2O_5, m-MTDATA, CuPc, C_{60}, Alq_3 and Al. All materials were deposited under pressure conditions of $4x10^{-6}$ mbar and deposition rates of 1-2 Å/s. Thickness was confirmed by ellipsometer. For characterization part, current density-voltage (J-V)

characteristics were measured using solar simulator with source meter. Fabrication and characterization was carried out in Centre for Nano Science and Engineering (CeNSE), Indian Institute of Science (IISc), Bangalore under Indian Nanoelectronics Users Program (INUP).

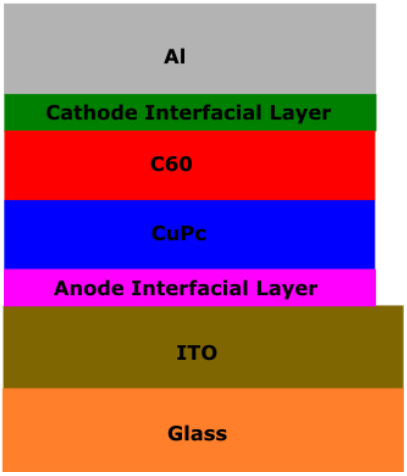

Figure 5.1: Schematic of the device. Here, anode interfacial layer is V_2O_5 or m-MTDATA 5 nm thicknesses and cathode interfacial layer is Alq_3 thickness is 5 nm or 10 nm

5.2 Results

This section presents the results obtained from the modeling using transfer matrix approach and the characterization of fabricated devices.

5.2.1 Optical electric field

Refractive index (n) and extinction coefficient (k) were extracted from ellipsometry. They were used in calculation of optical electric field intensity, device reflectance, power dissipation, absorptance and power redistribution. Thickness of layers were: ITO(150 nm)/AIL/CuPc(40 nm)/C60(40 nm)/CIL/Al(100 nm). Here AIL is V_2O_5 or m-MTDATA of 5 nm thickness and CIL is Alq_3 of 5 nm or 10 nm thickness.

Figure 5.2 (a) is the electric field distribution of device with V_2O_5 of 5 nm thickness as AIL and Alq_3 of 5 nm as CIL. For this device, electric field intensity peak lies within the active layer which is a desired requirement for maximizing efficiency of the device. In case of 10 nm thickness of Alq_3 electric field intensity peak, as shown in Figure 5.2 (b), lies within the active layer and the peak value higher by 0.23%.

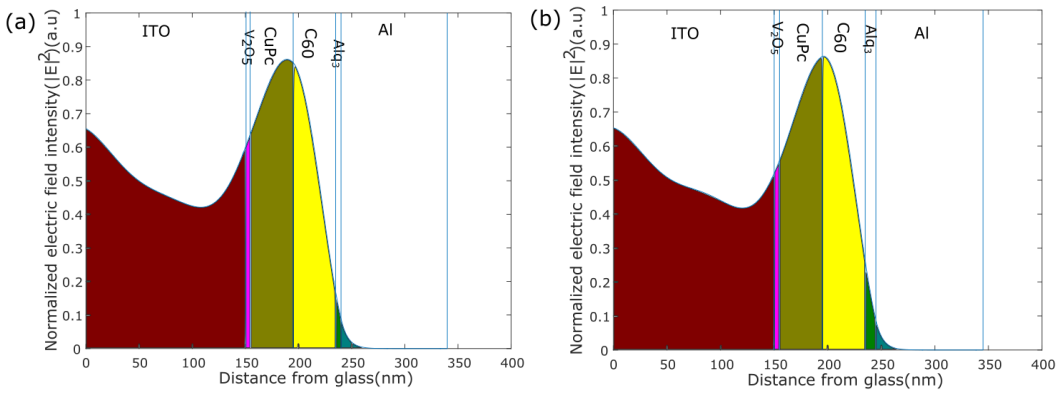

Figure 5.2: Optical electric field intensity distribution of device with V_2O_5 of 5 nm as AIL and Alq_3 as CIL of (a) 5 nm and (b) 10 nm thickness

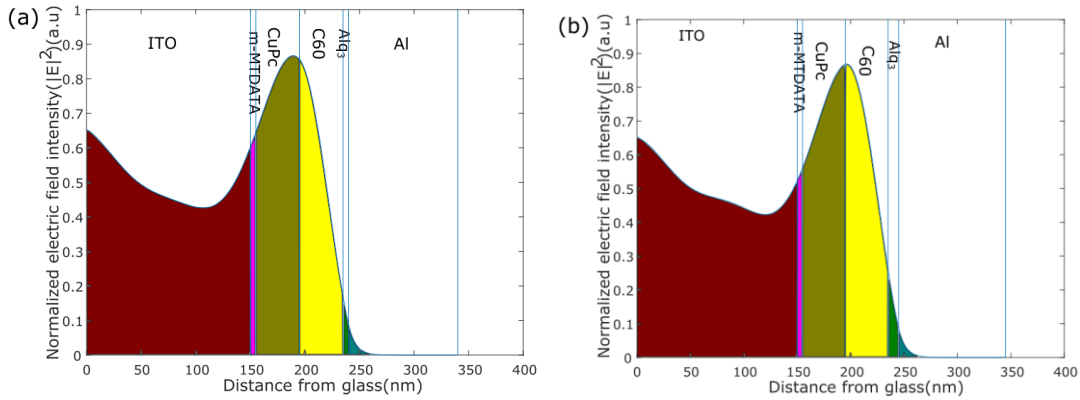

Figure 5.3: Optical electric field intensity distribution of device with m-MTDATA of 5 nm as AIL and Alq_3 as CIL of (a) 5 nm and (b) 10 nm thickness

Figure 5.3 (a) is electric field distribution of device with m-MTDATA of 5 nm as AIL and Alq_3 of 5 nm thickness as CIL. In case of 5 nm thickness of Alq_3 as CIL, electric field peak was higher by 0.54% for device with m-MTDATA as AIL compared to device with V_2O_5 as AIL. Figure 5.3 (b) is electric field distribution of device under m-MTDATA of 5 nm and Alq_3 of 10 nm thickness. In both cases, electric field intensity peak lies within the active layer and the peak value is higher by 0.27% compared to V_2O_5 of 5 nm. In case of 10 nm thickness Alq_3 as CIL, electric field peak was higher by 0.58% for device with m-MTDATA as AIL compared to devices with V_2O_5 as AIL. A shift in electric field intensity peak towards the left side of the interface between donor and acceptor was observed in case of devices with 5 nm thickness of Alq_3 compared to devices with 10 nm Alq_3.

5.2.2 Device reflectance

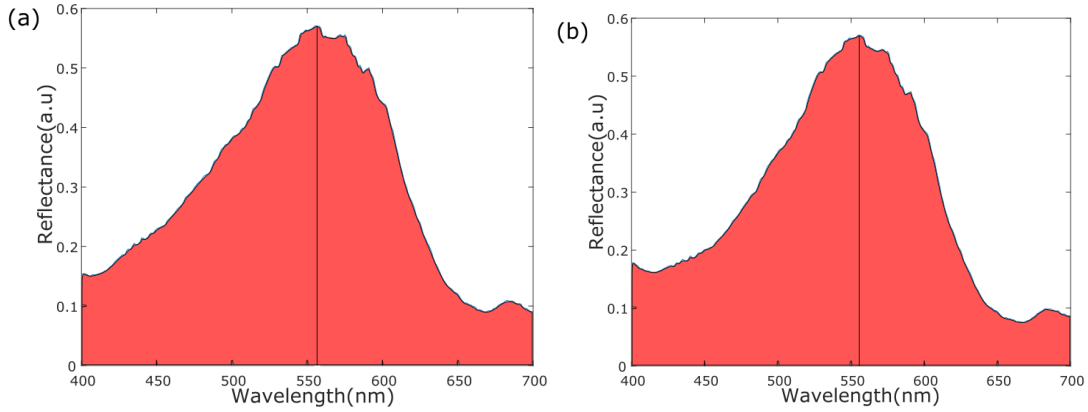

Figure 5.4: Reflectance of device with V_2O_5 of 5 nm as AIL and Alq_3 as CIL of (a) 5 nm and (b) 10 nm thickness.

Figure 5.4 (a) is reflectance of device with V_2O_5 of 5 nm thickness as AIL and Alq_3 of 5 nm thickness as CIL. The peak reflectance was observed near 550 nm wavelength. Figure 5.4 (b) is reflectance of device with V_2O_5 of 5 nm and Alq_3 of 10nm thickness. It was also observed that peak reflectance value was observed to be same in both cases.

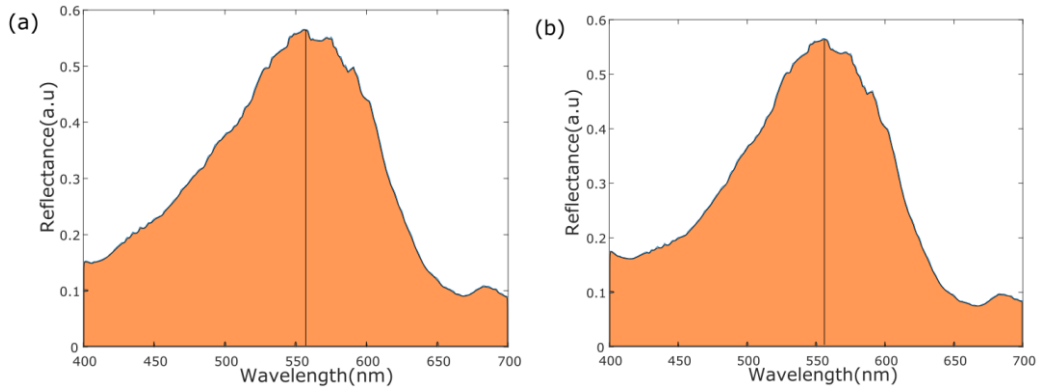

Figure 5.5: Reflectance of device with m-MTDATA of 5 nm as AIL and Alq_3 as CIL of (a) 5 nm and (b) 10 nm thickness.

Figure 5.5 (a) is reflectance of device with m-MTDATA of 5 nm thickness and Alq_3 of 5 nm thickness. The peak reflectance is lower for device with m-MTDATA as AIL compared device with V_2O_5 as AIL. Figure 5.5 (b) is reflectance of device with m-MTDATA of 5 nm thickness and Alq_3 10 nm. In both cases, peak reflectance was

observed to be same. The peak reflectance in these devices was observed around 550 nm wavelength.

5.2.3 Power dissipation

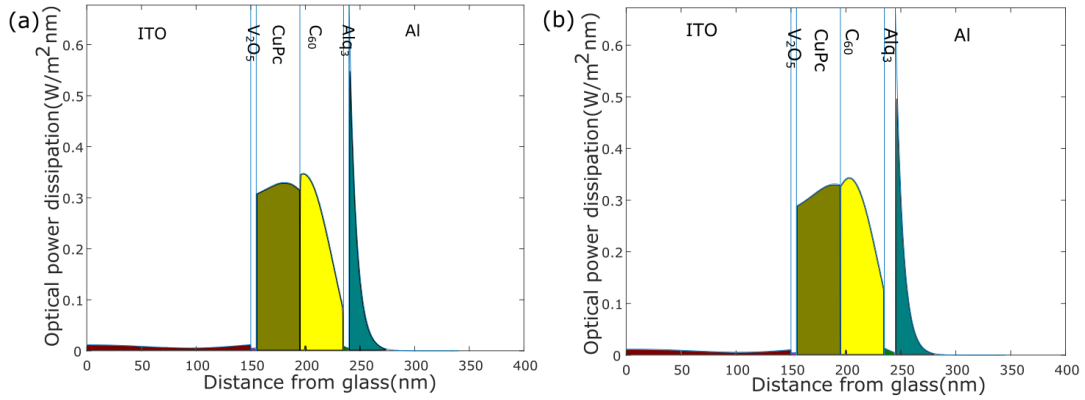

Figure 5.6: Power dissipation of device with V_2O_5 of 5 nm as AIL and Alq_3 of (a) 5 nm and (b) 10 nm thickness

Figure 5.6 (a) is power dissipation of device with V_2O_5 of 5 nm as AIL and Alq_3 of 5 nm thickness as CIL. It was observed maximum power dissipation is confined within the active layer materials of CuPc and C_{60}. Figure 5.6 (b) is power dissipation of device with V_2O_5 of 5 nm and Alq_3 of 10 nm thickness. Peak of power dissipation within the CuPc and C_{60} layers is near to CuPc:C_{60} interface, which is a desired requirement for maximization of efficiency of the device.

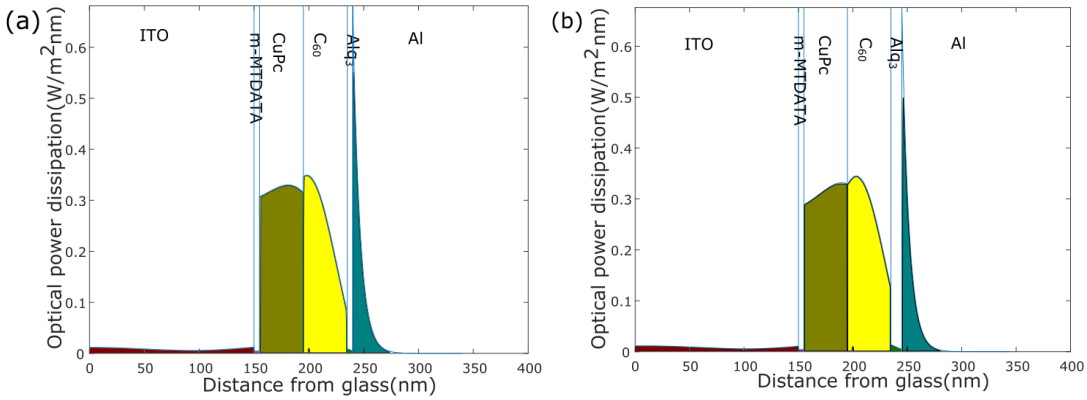

Figure 5.7: Power dissipation of device with m-MTDATA of 5 nm as AIL and Alq_3 as CIL of (a) 5 nm and (b) 10 nm thickness

Figure 5.7 (a) is power dissipation of device with m-MTDATA of 5 nm and Alq_3 of 5 nm thickness, measured using transfer matrix approach. In case of devices with

m-MTDATA as AIL, higher power dissipation in the active layer was observed compared to devices with V_2O_5 as AIL. Figure 5.7 (b) is power dissipation of device with m-MTDATA of 5 nm and Alq_3 of 10 nm thickness. Low power dissipation was observed in the interfacial layers which is a desired factor for consideration of interfacial layers.

5.2.4 Absorptance

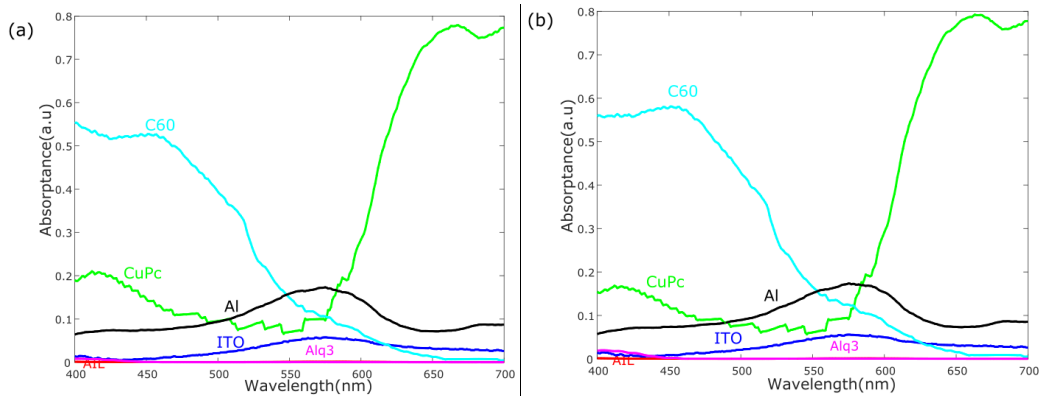

Figure 5.8: Absorptance of various layers of device with V_2O_5 of 5 nm as AIL and Alq_3 as CIL of (a) 5 nm and (b) 10 nm thickness

Figure 5.8 (a) is absorptance of various layers of device with V_2O_5 of 5 nm and Alq_3 of 5 nm thickness. From the absorptance curves, it was observed that CuPc material is absorbing higher wavelengths and C_{60} material is absorbing lower wavelengths. Figure 5.8 (b) is absorptance of various layers of device with V_2O_5 of 5 nm and Alq_3 of 10 nm thickness. With increase in thickness of Alq_3 absorptance increased in C_{60} layer and decreased in CuPc layer.

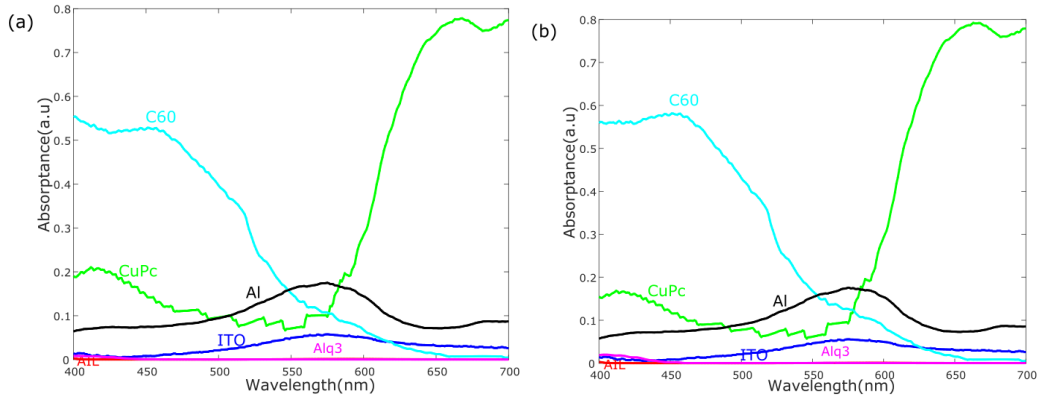

Figure 5.9: Absorptance of various layers of device with m-MTDATA of 5 nm as AIL and Alq_3 as CIL of (a) 5 nm and (b) 10 nm thickness

Figure 5.9 (a) is absorptance of various layers of device with m-MTDATA of 5 nm and Alq_3 of 5 nm thickness, measured using transfer matrix approach. Higher absorptance was observed in active layer materials of CuPc and C_{60} in case of devices with m-MTDATA as AIL compared to devices with V_2O_5 as AIL. Figure 5.9 (b) is absorptance of various layers of device with m-MTDATA of 5 nm and Alq_3 of 10 nm thickness. With increase in thickness of Alq_3 absorptance increased in C_{60} layer and decreased in CuPc layer.

5.2.5 Power redistribution

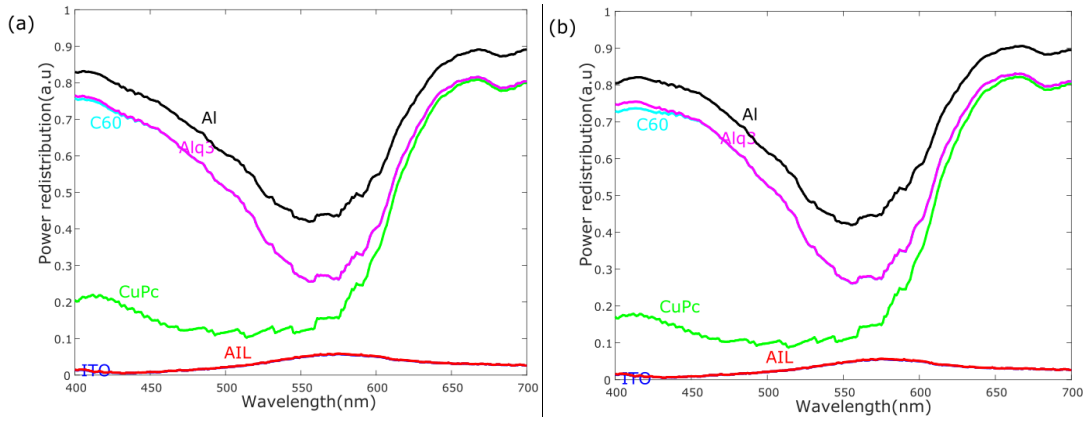

Figure 5.10: Power redistribution of device with V_2O_5 of 5 nm as AIL and Alq_3 as CIL of (a) 5 nm and (b) 10 nm thickness

Figure 5.10 (a) is power redistribution of device with V_2O_5 of 5 nm and Alq_3 of 5 nm thickness, measured using transfer matrix approach. Power redistribution curves shows how incoming energy is shared across different layers of the device as a function of wavelength. It can observed that share of energy within the interfacial layers is low. Figure 5.10 (b) is power redistribution of various layers of device with V_2O_5 of 5 nm and Alq_3 of 10 nm thickness. It was observed that with increase in thickness, the share of energy within the Alq_3 increased. It was also evident that CuPc layer is sharing higher wavelengths and C_{60} layer is sharing the lower wavelengths of incoming energy.

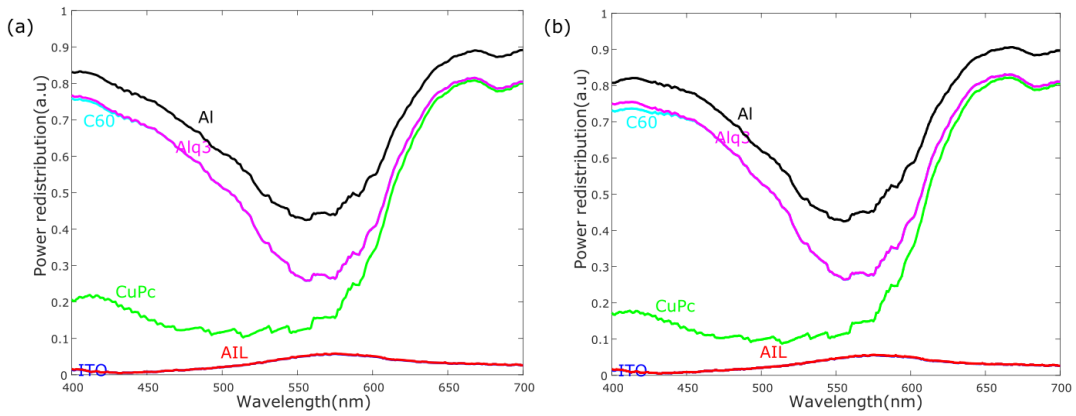

Figure 5.11: Power redistribution of device with m-MTDATA of 5 nm as AIL and Alq_3 as CIL of (a) 5 nm and (b) 10 nm thickness

Figure 5.11 (a) is power redistribution of device with m-MTDATA of 5 nm and Alq_3 of 5 nm thickness. Higher absorption in the active layer materials was observed in devices with m-MTDATA as AIL when compared devices with V_2O_5 as AIL. Figure 5.11 (b) is power redistribution of various layers of device with m-MTDATA of 5 nm and Alq_3 of 10 nm thickness. From power re-distribution curves, the remaining part above aluminum layer can be considered as reflectance of the device.

5.2.6 Electrical characterization

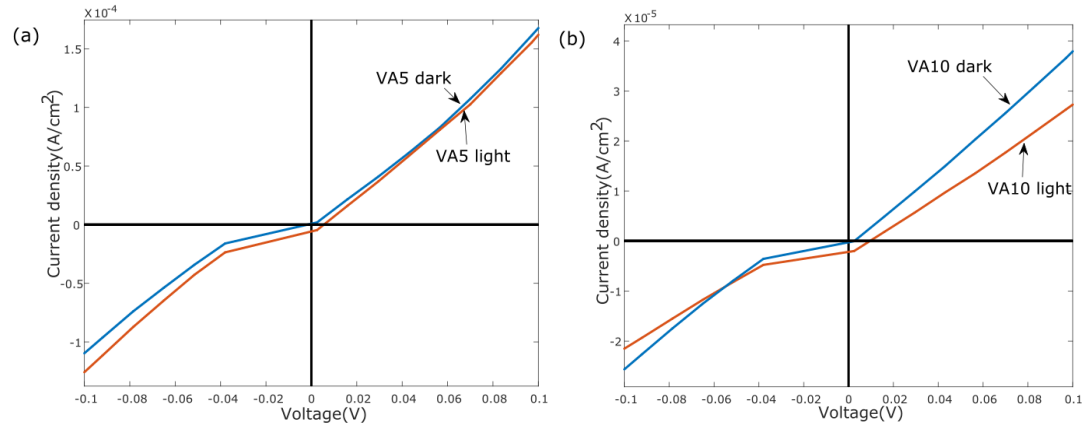

Figure 5.12: J-V characteristics of device with V_2O_5 of 5 nm as AIL and Alq_3 as CIL of (a) 5 nm and (b) 10 nm thickness under dark (blue line) and AM 1.5 solar simulation (red line) conditions

Figure 5.12 (a) is J-V characteristics of the device with V_2O_5 of 5 nm thickness as AIL and Alq_3 of 5 nm thickness as CIL under dark and light conditions. Open circuit voltage (V_{OC}) of 5.12 mV and short circuit current density (J_{SC}) of 5.524

$\mu A/cm^2$ was obtained in this case. The values of J_{SC} and V_{OC} are tabulated in Table 5.1 for comparative analysis of influence of CIL. Figure 5.12 (b) is J-V characteristics of the device with V_2O_5 of 5 nm thickness as AIL and Alq_3 of 10 nm thickness as CIL under dark and light conditions. V_{OC} of 9.74 mV and J_{SC} of 2.261 $\mu A/cm^2$ was obtained in this case. Lower J_{SC} and higher V_{OC} were obtained in device with Alq_3 of 10 nm thickness compared device with 5 nm Alq_3.

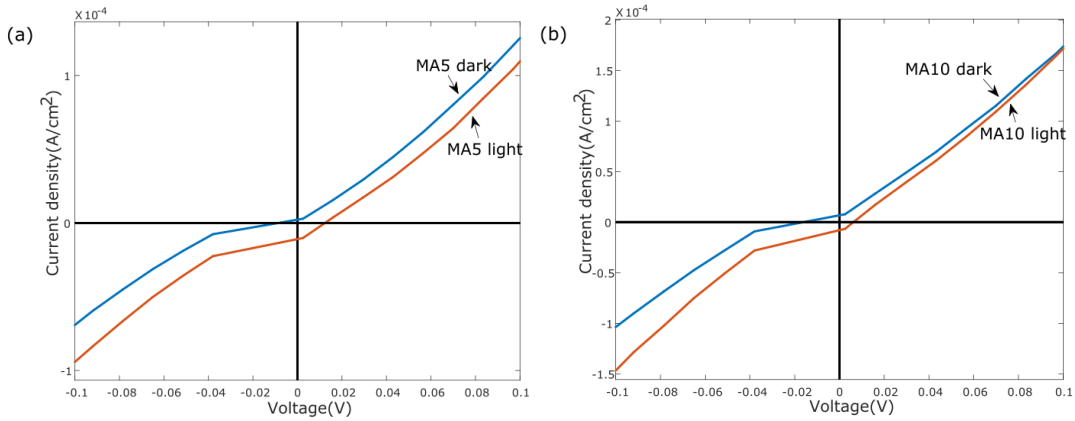

Figure 5.13: J-V characteristics of device with m-MTDATA of 5 nm as AIL and Alq_3 as CIL of (a) 5 nm and (b) 10 nm thickness under dark (blue line) and AM 1.5 solar simulation (red line) conditions

Figure 5.13 (a) is J-V characteristics of the device with m-MTDATA of 5 nm thickness as AIL and Alq_3 of 5 nm thickness as CIL under dark and light conditions. V_{OC} of 12.05 mV and J_{SC} of 10.48 $\mu A/cm^2$ were obtained. In case of devices with Alq_3 of 5nm thickness as CIL, higher J_{SC} and higher V_{OC} was obtained from devices with m-MTDATA as AIL compared to devices with V_2O_5 as AIL. Figure 5.13 (b) is J-V characteristics of the device with m-MTDATA of 5 nm thickness as AIL and Alq_3 of 10 nm thickness as CIL under dark and light conditions. V_{OC} of 6.15 mV and J_{SC} of 7.967 $\mu A/cm^2$ were obtained in this case. Lower V_{OC} and lower J_{SC} was observed in devices with 10 nm Alq_3 compared to devices with 5 nm Alq_3.

Device	J_{SC} ($\mu A/cm^2$)	V_{OC} (mV)
VA5	5.524	5.12
VA10	2.2609	9.74
MA5	10.483	12.05
MA10	7.967	6.15

Table 5.1: Open circuit voltage and short circuit density values measured from analysis of cathode interfacial layer. V denotes V_2O_5 of 5 nm, M denotes m-MTDATA of 5 nm and A5 denotes Alq3 of 5 nm.

5.3 Conclusions

From the modeling results, it was observed that devices with m-MTDATA as AIL showed higher electric field intensity peak compared with devices with V_2O_5 as AIL for both thicknesses of 5 nm and 10 nm of Alq_3. A shift in electric field intensity peak towards the left of interface of CuPc and C_{60} was observed in case of devices with 5 nm thickness of Alq_3. The reflectance peak is lower for devices with m-MTDATA as AIL compared to devices with V_2O_5 as AIL for both thicknesses of 5 nm and 10 nm of Alq_3. The peak reflectance remained the same with increase in thickness of Alq_3 and it was around 550 nm wavelength. The observations of higher electric field intensity peak and lower reflectance for devices with m-MTDATA as AIL can be correlated with higher short circuit current density for devices with m-MTDATA compared to devices with V_2O_5 as AIL. From the power dissipation measurements, it was known that maximum power dissipation is confined within the active layer materials of CuPc and C_{60}. From the absorptance measurements, CuPc had shown absorptance of higher wavelengths and C_{60} had shown absorptance of lower wavelengths.

From the current density-voltage characterization, it was observed devices with 5 nm thickness of Alq_3 as CIL resulted in higher J_{SC} compared to devices with 10 nm

Alq_3, whether the AIL is V_2O_5 or m-MTDATA. Devices with m-MTDATA as AIL showed higher J_{SC} and higher V_{OC} compared to devices with V_2O_5 as AIL for the devices with Alq_3 of 5 nm thickness.

Chapter 6

Conclusions and Future Work

6.1 Conclusions

The main focus of this thesis is to analyze the influence of interfacial layers in small molecule organic solar cells in order to improve efficiency and stability of the devices. Optical electric field, reflectance, power dissipation, absorptance and power re-distribution were determined using transfer matrix modeling. Fabrication of devices was done using thermal evaporation process. Electrical characterization was done for measurement of current density-voltage characteristics. Optical characterization was done to measure reflectance, thickness, reflection coefficient and extinction coefficient. The device schematic considered for the experiments is Anode(ITO)/Anode interfacial layer (V_2O_5, m-MTDATA)/Donor (CuPc)/Acceptor (C_{60})/Cathode interfacial layer (Alq_3)/Cathode (Al). Two materials, Vanadium oxide (V_2O_5) and 4,4',4''-Tris[(3-methylphenyl)-phenylamino]triphenylamine (m-MTDATA) were considered for analysis of influence of AIL and two thicknesses of 5nm and 10nm were considered in this experiment. Alq_3 material was considered for analysis of influence of cathode interfacial layer and two thicknesses of 5nm and 10nm were considered.

From the modeling and characterization, it was observed that devices with 5 nm thickness of anode and cathode interfacial layer showed better performance than devices with 10 nm thickness at. Devices with m-MTDATA as anode interfacial layer performed better than devices with V_2O_5 as anode interfacial layer.

6.2 Future work

In the present thesis, optical modeling was done for analyzing the influence of anode and cathode interfacial layers in small molecule organic solar cells based on CuPc and C_{60} materials. Optical electric field, reflectance, power dissipation, absorptance and power redistribution were measured by using transfer matrix approach. Electrical modeling can be done to analyze the influence of interfacial layers in small molecule organic solar cells.

For the present work, single material of V_2O_5 or m-MTDATA and Alq_3 was used as anode and cathode interfacial layer respectively. This work can be extended by using double and composite layers with two or more materials as interfacial layer in bulk heterojunction devices.